[A01]

The 2026 International Workshop on the High Energy Circular Electron Positron Collider (CEPC2026), ShangHai, China, Oct 21-26, 2026

*Development of 1.2 Mega-Watt P-band Travelling Wave Resonant Ring**

F.Y. Wang[1,2], Z.S. Zhou†[1,2], O.Z. Xiao[1], N. Gan[1], J.D. Liu[1]

[1]Institute of High Energy Physics, Chinese Academy of Sciences, Beijing 100049, China

[2]University of Chinese Academy of Sciences, Beijing 100049, China

中国科学院高能物理研究所
Institute of High Energy Physics
Chinese Academy of Sciences

ABSTRACT

The reliable operation of high-power RF components, including superconducting cavity input couplers and RF windows, is critical for accelerator facilities. Prior to installation into accelerator systems, these components typically require high-power conditioning to verify their RF performance and thermal stability. However, establishing megawatt-level RF test facilities is challenging due to the complexity and limited availability of high-power RF sources.To address this challenge, the Institute of High Energy Physics (IHEP) has developed a 650 MHz traveling-wave resonant ring (TWRR) system,which enables megawatt-level circulating power by accumulating RF energy in a closed-loop structure with a relatively low-power RF source.The system was tested under high-power continuous-wave(CW) operation. A circulating power of approximately 1.2 MW was achieved with an injected RF power of only 42.7 kW.Stable CW operation was maintained for 8 h without interruption.These results demonstrate the feasibility of MW-level CW RF conditioning using a TWRR and provide an effective test platform for future CEPC RF components.

INTRODUCTION

Because high-power RF sources above the megawatt level are expensive and difficult to operate, resonant-ring technology,which has been investigated since the 1960s[1], provides an economical solution for high-power RF components qualification.Previous studies have demonstrated significant power enhancement in different frequency bands.However, megawatt level continuous-wave operation of large-aperture WR1500 waveguide-based TWRR systems for accelerator component conditioning has rarely been reported.The Institute of High Energy Physics (IHEP) has developed a 650 MHz P-band WR1500 TWRR for high-power RF components conditioning.

PRINCIPLE

The basic configuration of a traveling-wave resonant ring is illustrated in Fig. 1.The TWRR is a feedback system that uses a main directional coupler to inject RF power into a closed waveguide loop.With the appropriate ring length and matching,these waves add constructively, resulting in a voltage increase that functions as power gain within the ring.

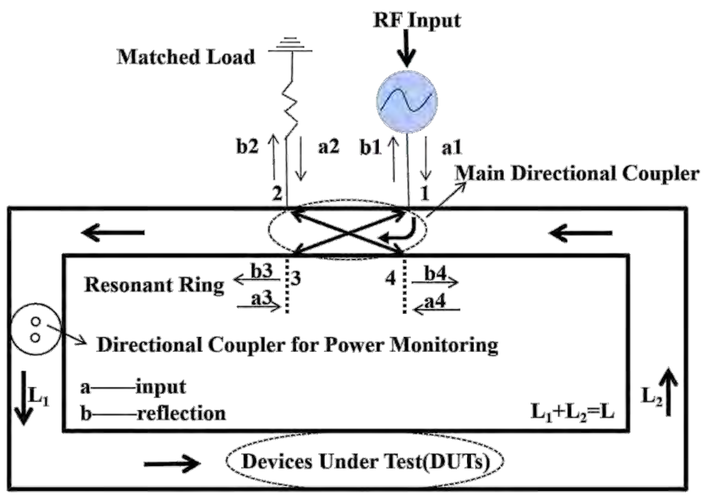


Figure 1: Schematic Diagram of a TWRR.

FOMULA

Under the resonance condition,the theoretical power gain of the TWRR can be expressed as[2]:

$$G = \left|\frac{b_3}{a_1}\right|^2 = \frac{C^2}{(1-\sqrt{1-C^2}\cdot e^{-\alpha l_0})^2} \quad .$$

where G is the circulating power gain, C is the power coupling coefficient of the main directional coupler, α is the attenuation constant of the waveguide, and l0 is the total length of the resonant loop.

COMPONENTS OF P-BAND TWRR

The 650 MHz P-band TWRR was designed based on a WR1500 waveguide structure. The system mainly consists of a 10dB main directional coupler(left in Fig. 2), a 60.73dB power-monitoring coupler(right in Fig. 2), a mechanical phase shifter(right in Fig. 2) and other waveguide sections.

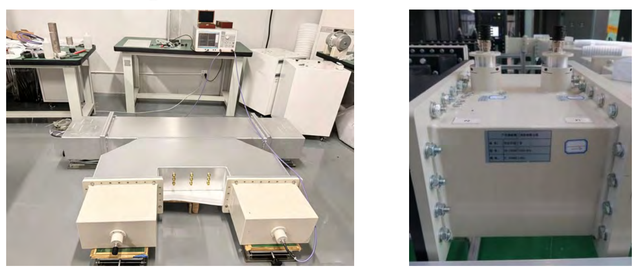


Figure 2:10 dB Coupler(left) , 60.73 dB Couple(right).



Figure 3:Phase Shifter.

CONFIGURATION OF P-BAND TWRR

Configuration of the P-band TWRR system is showed in Fig4. The RF source used in the experiment is a 650 MHz, 150 kW solid-state power amplifier, with only two amplifier modules during the test.

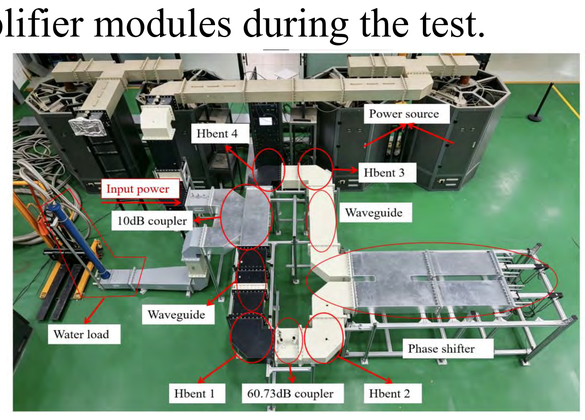


Figure 4: Configuration of the P-band TWRR System.

HIGH POWER OPERATION OF P-BAND TWRR

A circulating power of approximately 1.2 MW was obtained with an input power of 42.7 kW. The system operated stably for 8 h, as shown in Fig.5.

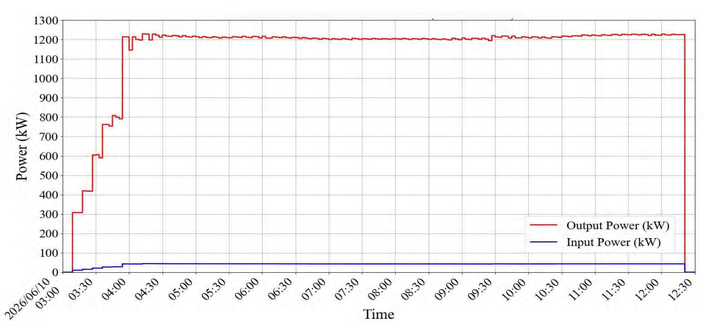


Figure 5: Power Performance of the P-band TWRR.

HIGH-POWER OPERATION OF P-BAND TWRR(Continued)

A summary of the parameters of the P-band TWRR is provided in Table 1.

Table 1 Results of P-band TWRR

Parameter	Value
Frequency[MHz]	650
Waveguide	WR1500
Input power [kW]	42.7
Circulating power [MW]	1.2
Gain(high-power operation) [dB]	14.5

Thermal management was implemented using a combination of forced-air cooling and local heat dissipation enhancement.The maximum surface temperature exceeded 80° C and was mainly observed around the phase shifter (as shown in Fig.6).

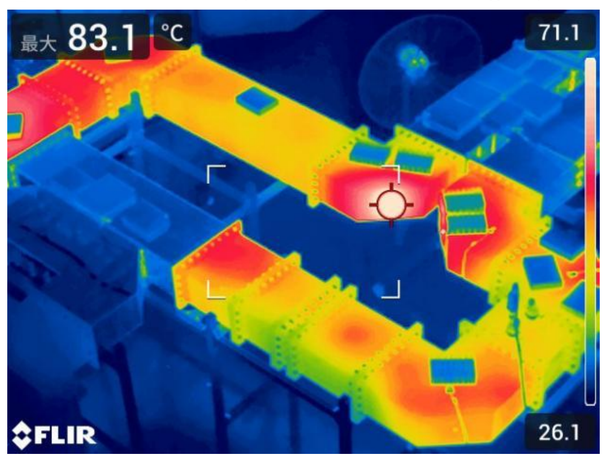


Figure 6: Temperature Rise of P-band TWRR.

SUMMARY AND OUTLOOK

The developed system provides an efficient platform for conditioning and qualification of high-power RF components, such as the 650 MHz ceramic windows for the CEPC[3] RF system and RF couplers. The RF power can be gradually increased by adjusting the input power while maintaining the phase closure condition using the phase shifter. Key parameters, including forward and reflected power, component temperature can be monitored throughout the process.

REFERENCES

[1]K. Jin and N. Holtkamp, “S-Band Resonant-Ring at DESY”, DESY M 96-11, 1996.

[2]L.J. Milosevic and R. Vautey, “Traveling-wave resonators”, IRE Trans. Microwave Theory Tech.,vol.6,no.2,pp. 136-143, 1958.

[3]J. Gao, "CEPC Technical Design Report: Accelerator," Radiat. Detect. Technol. Methods, vol. 8, pp. 1–1105, 2024, doi: 10.1007/s41605-024-00463-y.

*** Work supported by Yifang Wang’s Science Studio of the Thousand Talents Project and National Key Programme for ST Research and Development (Grant NO.: 2024YFA1610602)**

† email address: zhouzs@ihep.ac.cn

[A02]

The 2026 International Workshop on the High Energy Circular Electron Positron Collider (CEPC2026), Shanghai, China, Oct 22-26, 2026

Development of high voltage pulsed modulator for the CEPC C band 80MW Klystron

Fei Li[1] , Dayong He[1,2] , Jindong Liu[1,2] , Nan Gan[1,2], Yajie Mu[1] , Yuying Ding[1,2] , Zusheng Zhou[1.2†]

1Institute of High Energy Physics, Chinese Academy of Sciences, Beijing 100049

2University of Chinese Academy of Sciences, Beijing 100049, China

中国科学院高能物理研究所
Institute of High Energy Physics
Chinese Academy of Sciences

High-voltage pulse modulator is a key device in linear accelerators, serving as the intermediate link that converts power from the power supply into microwave power. According to the CEPC technical design, the linear accelerator requires 236 sets of C-band 80 MW power source systems to supply 5712 MHz/3 μs/100 Hz pulsed power to the accelerating structures. To achieve the target klystron output power of 80 MW, the high-voltage pulse modulator must deliver pulsed voltages of 425 kV, pulsed currents of 425 A, and a minimum output power of 180 MW. The pulse rise and fall times directly determine the modulator's efficiency, while repetition stability critically influences beam quality. The 100 Hz repetition rate imposes stringent requirements on power handling capacity and thermal management. To meet these challenges, a high-voltage pulse modulator based on a solid-state topology has been developed specifically for C-band 80 MW applications. This paper presents the current development progress from several aspects, including the comprehensive circuit calculation of the high-voltage pulse modulator, theoretical analysis and structural design of the pulse transformer, and simulation analysis.

INTRODUCTION

The structural layout of the CEPC Linac is shown in Fig.1. Its RF power source system consists of 33 sets of 80 MW pulsed klystrons operating at 2860 MHz (S-band) and 236 sets of 80 MW pulsed klystrons operating at 5720 MHz (C-band). Among them, each C-band 50 MW klystron supplies power to two 1.8 m accelerating structures, which operate at an accelerating gradient of 45 MV/m. To make the linac more compact, it is proposed to upgrade the C-band 50 MW klystrons to 80 MW klystrons. After the design is completed, a single 80 MW klystron can supply power to four 1.8 m accelerating structures, reducing the overall cost of the linac by approximately 30%. The fabrication of the C-band 80 MW klystrons started in October 2024, and high-power tests will be conducted by the end of 2025. The parameters of the C-band 50 MW/80MW klystron are presented in Table 1.

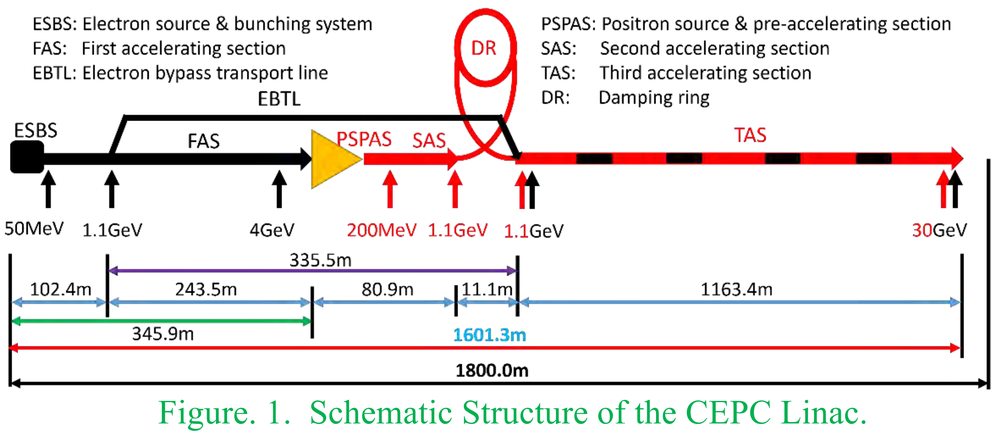


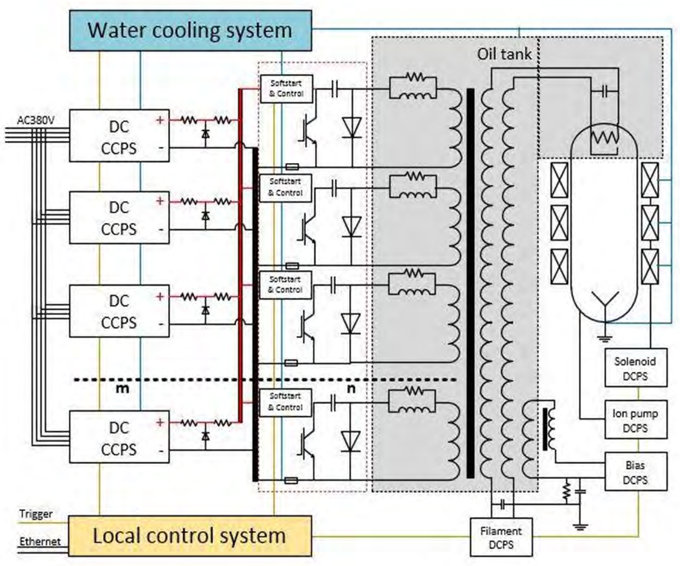
Figure. 1. Schematic Structure of the CEPC Linac.

Table. 1. Parameters of the C-band 50 MW/80MW Klystron

Parameters	**50 MWKlystron**	**80MW Klystron**
Output Power (MW)	50	80
Beam Voltage (kV)	350	425
Beam Current (A)	317	425
Efficiency (%)	48	47
Gain (dB)	＞50	＞50

SOLID-STATE MODULATOR

The high-voltage pulse modulator is a key device of the linear accelerator, acting as an intermediate link for converting electrical energy into microwave power. With the rapid iteration of solid-state power electronics technology, solid-state modulators featuring semiconductor devices as the core have demonstrated comprehensive advantages over the traditional PFN pulse power technology: they not only offer higher output stability and a more compact structure but also possess a much longer service life than thyratrons. This solid-state modulator consists of a high-precision direct current (DC) power supply, energy storage capacitors, IGBTs, low-inductance cables, and a matrix pulse transformer, whose schematic diagram is shown in Figure 2.



Figue.2. Schematic Diagram of the Solid-State Modulator.

Table. 2. Parameters of the C-band 80 MW Klystron

Parameters	**50 MWKlystron**
Pulse Voltage (kV)	430
Pulse Current (A)	440
Repetition Frequency (pps)	100
Pulse Width (μs)	3
Pulse Flat-Top Stability (%, within 4 μs)	1
Pulse Stability (%, over 3000 pulses)	0.02

For the C-band 5720 MHz/50 MW/100 pps/3 μs klystron load, the design parameters of its solid-state modulator are presented in Table 2. The solid-state modulator for the C-band 80 MW klystron has a pulse top width of 3 μs, a rise time and fall time of approximately 1.8 μs, resulting in a full width at half maximum (FWHM) of 4.4 μs for the pulse, and the average power of the DC power supply unit is 90.8 kW.

To ensure system redundancy, commercial 1,700 V IGBTs are adopted as switches for the discharge units, operating under the conditions of 1,000 V DC and 2,000 A. All discharge units work together, with a total current of 211 kA from 108 units. To control the pulse flatness within 1% over 3 μs, a parallel LR compensation circuit is specifically added to the discharge units. The pulse transformer of the solid-state modulator employs a biconical high-voltage winding to construct the DC current loop for the klystron cathode filament. The high-frequency characteristic $(L\delta/Cd)^{1/2}$ of the pulse transformer is determined by the leakage inductance Lδ and distributed capacitance Cd, which must be accurately matched to the impedance of the klystron.

REFERENCES

[1] The CEPC Study Group. CEPC Technical Design Report: Accelerator[J]. Radiation Detection Technology and Methods, 2024, 8(1).
[2] I. A. Guzilov, “BAC method of increasing the efficiency in klystrons”, s10th Int. Vacuum Elec. Sources Conf. (IVESC ’14), Saint Petersburg, Russia, July 2014.
[3] R. V. Egorov, I. A. Guzilov, “BAC-klystron: a new genera-tion of klystrons in vacuum electronics”, MOSCOW UNI-VERSITY PHYSICS BULLETIN, 2019, Vol. 74, No. 1, pp 38-42
[4] G. Burt et al., “Particle-in-cell simulation of a core stabiliza-tion method klystron”, IEEE International Vacuum Electronics Conference. (IVEC 2017), London, UK, April, 2017.
[5] IEEE Std 390TM-2007，IEEE Standard for Pulse Transformers.

*** Work supported by Yifang Wang’s Science Studio of the Thousand Talents Project**

† email address: zhouzs@ihep.ac.cn

[A03]

Development of high power energy recovery absorbing load for large scale accelerators

A03

Yang Zhao[1,2], Xiang He[1,2], Fei Li[1,2],Wenbin Gao[1,2],Jindong Liu[1,2], Ouzheng Xiao[1,2], Nan Gan[1,2], Yongliang Zeng[1,2], Zusheng Zhou[1,2]*

[1]Institute of High Energy Physics, Chinese Academy of Sciences, Beijing, China
[2]University of Chinese Academy of Sciences, Beijing, China

中國科學院高能物理研究所
Institute of High Energy Physics
Chinese Academy of Sciences

Abstract

For large particle accelerators, the radio-frequency (RF) power source system accounts for a significant portion of total energy consumption. A considerable fraction of the RF power that is not used for particle acceleration is delivered to an absorbing load located at the output of the accelerating structure, where it is converted into heat and dissipated. Recovering this otherwise wasted energy is therefore of great interest for improving the overall energy efficiency of accelerator facilities.

RF-DC rectification technology offers a potential approach to convert the RF power into usable DC electricity. However, the practical implementation of this concept has long been limited by insufficient high-frequency and high-power handling capabilities of conventional semiconductor devices. As a result, although the concept is attractive, it has rarely been demonstrated in experimental or engineering applications at the GHz frequencies.

With the recent development of Gallium Nitride (GaN) transistors, significant improvements in high-frequency and high-power performance have been achieved, making RF energy recovery at microwave frequencies more feasible.This work investigates the feasibility of GaN-based RF rectification and its potential for improving energy efficiency in future colliders like the CEPC and BEPCII, the energy loss of the s-band power source system is shown in the Fig. 1.

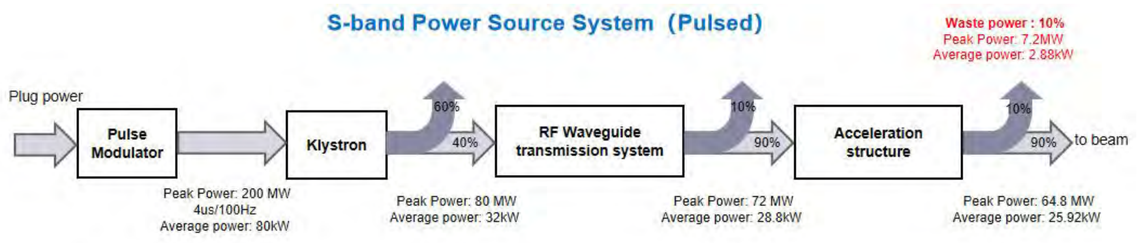


Fig. 1.Power-flow distribution in a pulsed S-band RF source system, illustrating the RF power not delivered to the beam as a potential source for energy recovery.

Energy-recovery absorbing-load architecture

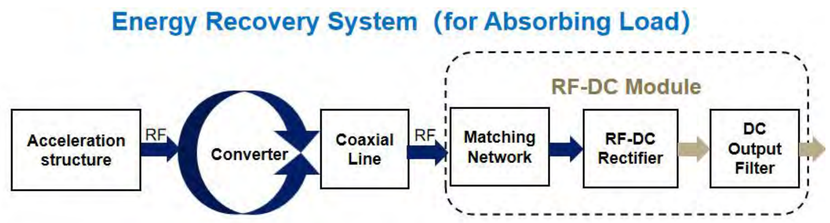


Fig. 2. Functional chain:
accelerating structure → RF extraction and transport → impedance matching → GaN RF–DC rectification → DC-output filtering.

The proposed energy-recovery absorbing load consists of two integrated subsystems: a microwave-extraction-and-transmission section and a core RF–DC rectification section.

The microwave-extraction section couples recoverable RF power from the accelerating structure and transfers it to the rectifier through a waveguide-to-coaxial transition and an impedance-matching interface. Its role is to establish an efficient RF link between the accelerator-side absorbing-load environment and the rectification circuit.

The RF–DC rectification section is the core of the system. It employs a GaN-based rectifier together with matching, bias, and DC-filtering networks to convert the extracted microwave power into usable DC power. The interface between the two subsystems must be co-designed to ensure effective power transfer while avoiding excessive reflected power toward the accelerating structure.

Microwave-extraction circuit design

Design Concept

The microwave-extraction device is designed to route unused RF energy remaining at the downstream end of the accelerating structure into a subsequent rectification circuit. Within the accelerating structure, RF energy propagates as guided electromagnetic waves and therefore cannot be fed directly into an RF rectifier. The extraction device is a specially designed waveguide-to-coaxial transition comprising a coupling plate, coupling aperture, and output port, as shown in Fig. 3a. By adjusting the insertion depth of the coupling plate, the extracted RF power can be continuously controlled, enabling the device to interface with RF rectifiers designed for different input-power levels.

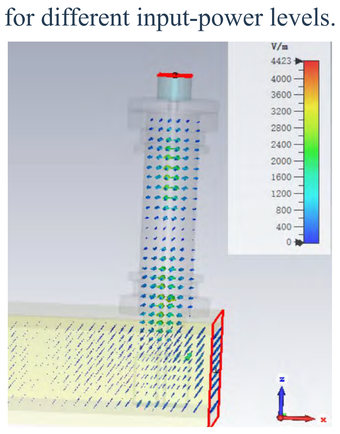


Fig. 3a. EM model used to assess extraction coupling and field distribution.



Fig. 3b. Microwave-extraction hardware used in the prior system study.

Simulation Results

CST simulation results show that the extraction structure provides controllable coupling over the investigated tuning range while maintaining low input reflection.

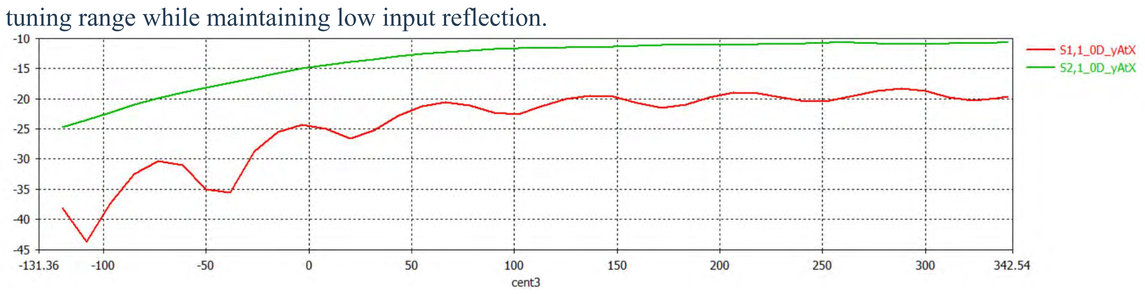


Fig. 4.CST-simulated S11 and S21 responses of the microwave-extraction structure over the investigated tuning range, demonstrating controllable RF extraction with low input reflection.

High-Power GaN RF–DC Rectifier Design

What's the difficulty?

- Owing to the limitations imposed by semiconductor material properties, high-power S-band RF rectification can currently be realized only with GaN devices; conventional SiC devices have exceeded their applicable power–frequency limits.
- The power-handling capability of GaN-based diodes remains relatively limited. Therefore, the rectifier topology must differ from that of conventional diode rectifiers.

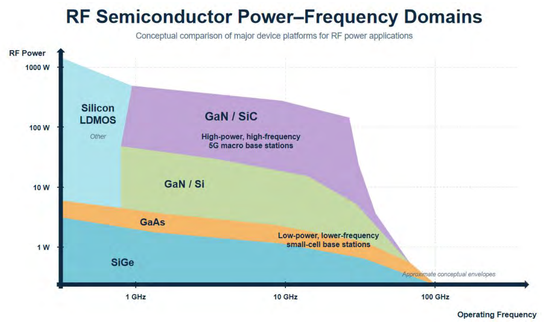


Fig. 5. Power–frequency operating domains of representative RF semiconductor technologies, highlighting the suitability of GaN devices for high-power S-band RF–DC conversion.

How to design an RF–DC module at high frequencies and high power levels

The practical circuit is implemented using dedicated input matching, gate matching and bias, drain harmonic-control, and DC-output networks. At S-band, these networks must be treated as an integrated electromagnetic system rather than as independent lumped elements. The drain-side RF port receives the extracted RF power, while a sampled and phase-adjusted signal is applied to the gate. The gate and drain networks establish the required impedance transformation and phase relationship, and the bias networks provide the DC operating conditions while isolating the RF paths. The final layout is refined through combined circuit and full-wave electromagnetic simulations.

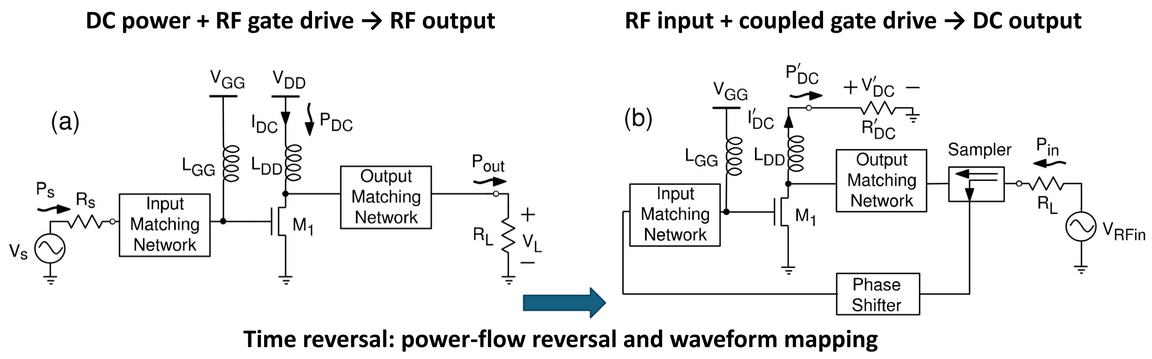


Fig. 6.Time-reversal duality between (a) a high-efficiency power amplifier and (b) the corresponding GaN HEMT RF–DC rectifier with a coupled, phase-adjusted gate drive.

The practical circuit is realized through dedicated input matching, gate matching and bias, drain harmonic control, and DC-output networks. At S-band, these networks must be treated as an integrated electromagnetic system rather than as independent lumped elements. The drain-side port receives the recovered RF power, whereas a sampled and phase-adjusted signal is applied to the gate. The gate and drain networks establish the required impedance transformation and phase relationship, while the bias networks provide the DC operating conditions and isolate the RF paths. The final layout is refined through combined circuit and full-wave electromagnetic simulations.

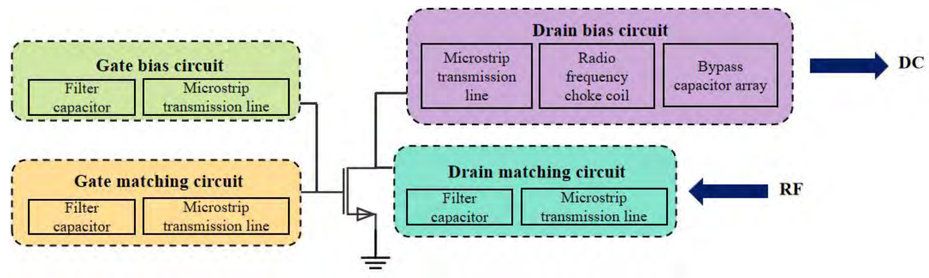
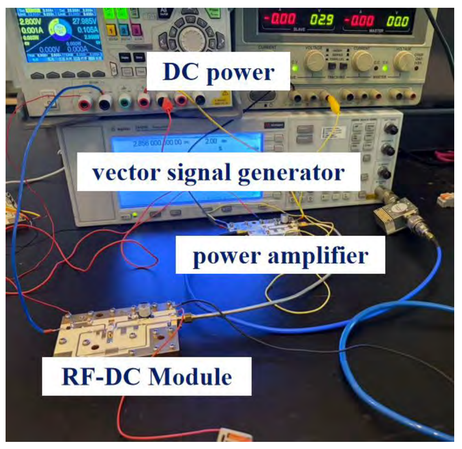


Fig. 7.Functional block diagram of the proposed RF–DC module, including the input matching, gate matching and bias, drain harmonic-control, drain-bias, and DC-output networks.

Experimental Validation

A CG2H40010F-based GaN HEMT RF–DC rectifier has been fabricated and tested. Preliminary continuous-wave measurements at 2.856 GHz demonstrate conversion of a 10 W RF input into DC power, verifying the basic operating principle of the proposed circuit.



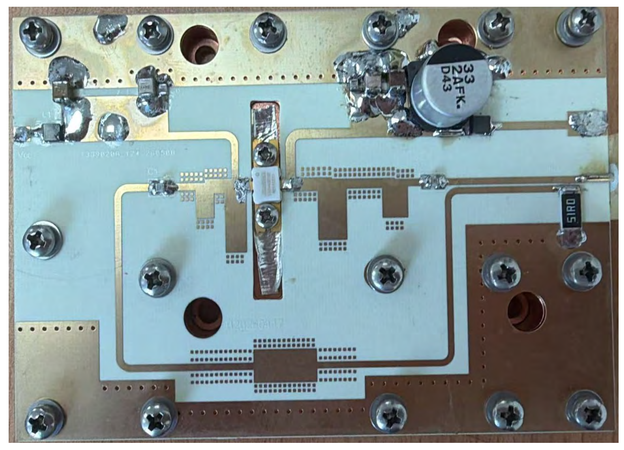


Fig. 8.Continuous-wave test setup (left) and fabricated CG2H40010F-based RF–DC rectifier prototype (right).

Conclusions

This work presents an energy-recovery RF–DC conversion approach for large-scale accelerators by combining microwave extraction and GaN HEMT rectification. A CG2H40010F-based RF–DC rectification module has been fabricated and preliminarily tested at 2.856 GHz with a 10 W RF input. Future work will investigate the mechanisms governing RF–DC conversion efficiency, refine the matching, bias, and harmonic-control networks, and conduct integrated tests of the microwave-extraction and rectification subsystems. Once the design methodology is validated, the approach will be extended to a 100-W-class RF–DC rectifier.

*** Work supported by Yifang Wang's Science Studio of the Thousand Talents Project and National Key Programme for ST Research and Development(Grant NO.: 2024YFA1610602)**

Contact: Yang Zhao | yangzhao@ihep.ac.cn

[A04]

The 2026 International Workshop on the High-Energy Circular Electron-Positron Collider(CEPC2026),Shanghai, China, Oct 23-27, 2023

*Coupling Mechanisms of Focusing Magnetic Field, Load Mismatch, and Electron Reflection in High-Power Klystrons**

Xiaobo zhou[1], Zusheng Zhou†[1], Ouzheng Xiao, Han Xiao[1]

Institute of High Energy Physics, Chinese Academy of Sciences, Beijing 100049, China

[1]also at University of Chinese Academy of Sciences, Beijing 100049, China

High-power klystrons play a critical role in radio-frequency (RF) systems for large-scale accelerators, where operational stability is essential for long-term reliability. This study investigates the coupled effects of focusing magnetic fields, load mismatch, and electron reflection on klystron performance and stability. A coupled analysis model incorporating beam transport, output-cavity complex loading, and backstreaming-electron feedback is established. Calculations show that, at a voltage standing-wave ratio (VSWR) of 1.2, different reflection phases can increase the output-cavity gap voltage by approximately 19.8% or decrease it by approximately 16.5% relative to the matched condition, assuming an approximately unchanged fundamental-frequency beam current. These results demonstrate that load-mismatch effects depend on both reflection magnitude and phase, providing a theoretical reference for output-cavity parameter optimization, focusing magnetic-field adjustment, and stability assessment.

INTRODUCTION

The analysis focuses on the output cavity and the coupled interactions among the focusing magnetic field, electron beam, and reflected RF power.Based on the relativistic equations of electron motion, the influence of the focusing magnetic field on beam transmission, electron bunching, and the fundamental-frequency beam current upstream of the output cavity is investigated.Combining the output-cavity equivalent-circuit model with transmission-line theory, the relationships among VSWR, reflection phase, normalized load admittance, equivalent external quality factor, loaded quality factor, and gap voltage are derived.Load mismatch modifies the effective loading and electromagnetic response of the output cavity, thereby changing the gap voltage and electron deceleration conditions. Under sufficiently strong decelerating fields, electron reflection may occur. Backstreaming electrons can introduce additional beam–cavity feedback, potentially contributing to parasitic oscillations when the relevant feedback conditions are satisfied.The focusing magnetic field further influences these processes by modifying beam transport and bunching characteristics. Consequently, the combined effects of magnetic focusing and complex load impedance should be considered when evaluating klystron performance, electron-reflection risks, and operating stability.

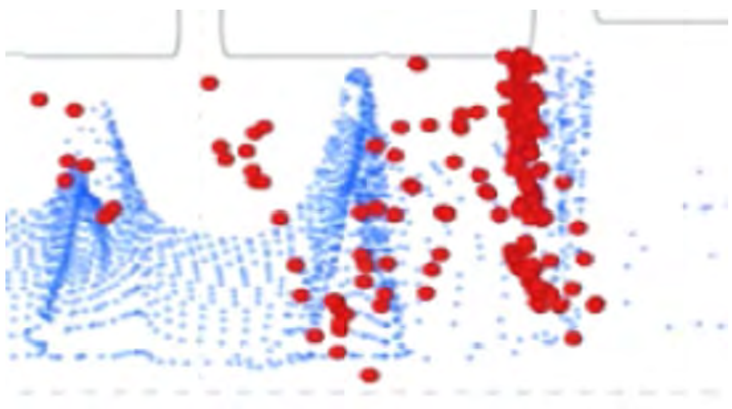


Figure 1:Reverse-flow electron diagram

THE EFFECTS OF LOAD MISMATCH

Load mismatch modifies the complex load admittance seen by the output cavity, thereby affecting its effective external quality factor and resonant frequency. The normalized conductance component (g) governs the dissipative loading, while the susceptance component (b) introduces an effective resonance-frequency shift. Under small-perturbation conditions, the relative change in external quality factor is approximately proportional to the negative conductance perturbation, whereas the relative frequency shift is proportional to the susceptance component. Consequently, even at the same voltage standing-wave ratio (VSWR), different reflection phases can produce different loading conditions and frequency detuning, leading to variations in gap voltage, beam–wave interaction, and RF conversion efficiency, and potentially affecting the operational stability of the klystron.

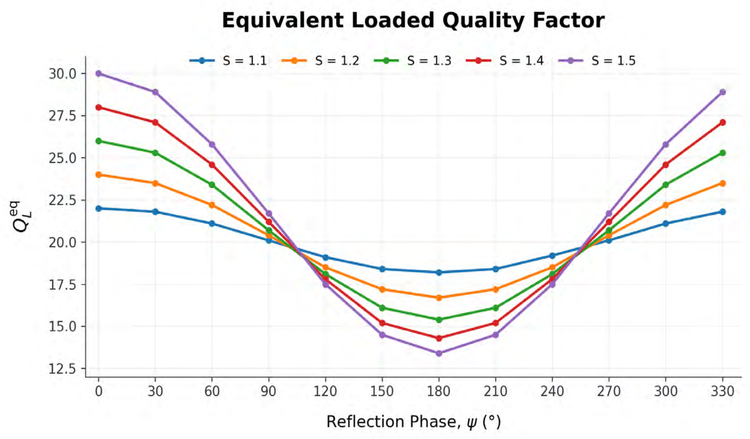


Figure 2:Effect of Load Mismatch on Loaded Quality Factor

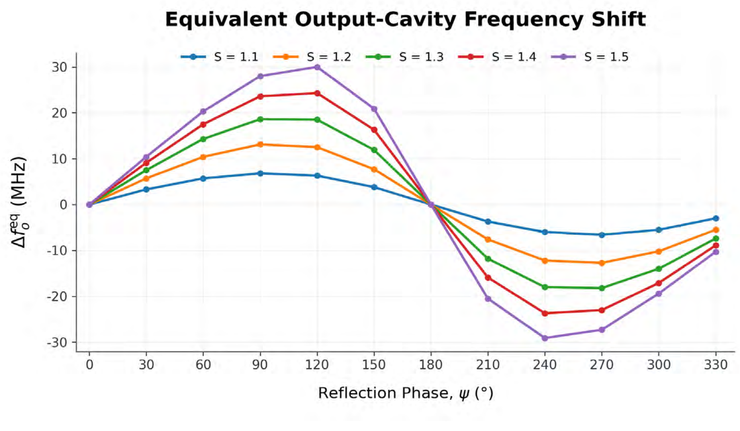
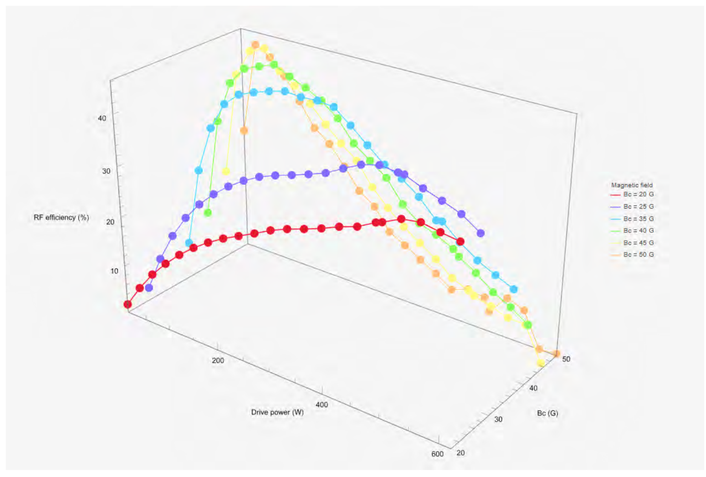


Figure 3:Effect of Load Mismatch on Frequency Shift

In fact, both the focusing magnetic field and RF drive affect the output power and stability by influencing the beam quality factor.



Therefore, we select an RF drive power of 160 W and a cathode magnetic field of 40 Gs as the nominal operating conditions.

Operating frequency	2856 MHz
Drive power	160 W
Beam voltage	289 kV
Beam current	321 A
Cathode magnetic	40 Gs

Table 1: Klystron parameters

Subsequently, simulations were conducted to investigate the effects of load mismatch, and the results are presented below.

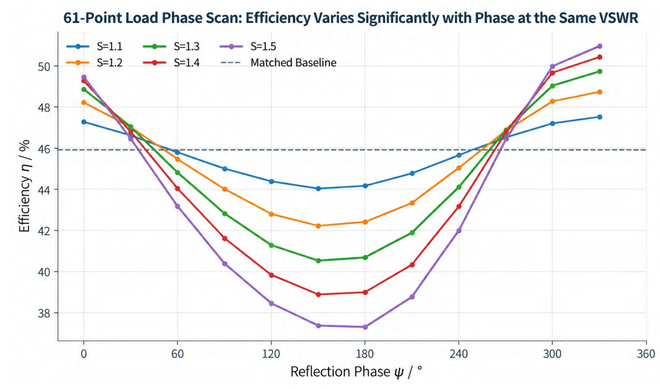


Figure 4:Effect of Load Mismatch on Efficiency

At an RF drive power of 160 W and a cathode magnetic field of 40 G, the effects of VSWR and reflection phase on klystron efficiency were investigated. The results show that efficiency varies significantly with reflection phase even at a fixed VSWR. As VSWR increases, efficiency becomes more sensitive to reflection phase. At VSWR = 1.5, the efficiency varies from approximately 37.3% to 51.0%, compared with about 45.9% under matched conditions. These results indicate that the effects of load mismatch depend on both reflection magnitude and phase, potentially through changes in the effective output-cavity impedance and gap voltage, which influence beam–wave energy transfer.

SUMMARY AND OUTLOOK

The results demonstrate that load mismatch significantly affects the output-cavity voltage, induced current, and efficiency through changes in the effective cavity impedance and loaded quality factor. These effects may also influence beam loading, electron reflection, and operational stability. Future work will focus on investigating the formation of backstreaming electrons, establishing self-oscillation criteria, and identifying critical instability conditions to improve the stability and reliability of high-power klystrons.

REFERENCES

[1]SINGH A, KONRAD G T, GRIFFIN C. Stability of klystron operation as a function of input parameters[R]. SLAC-TN-84-004, 1984.

[2]DING Y G, SHEN B, DING H B. Influence of load mismatch on output characteristics of klystron[J]. High Power Laser and Particle Beams, 2011, 23(5): 1319-1323.

[3] KRIETENSTEIN B, KO K, LEE T, et al. Spurious oscillations in high power klystrons[C]//Proceedings of the 1995 Particle Accelerator Conference. 1995: 1533-1535.

[4] HUANG H, CHEN Z F, YUAN H, et al. Research on stability of repetitive operation of S-band, long-pulse relativistic klystron[J]. High Power Laser and Particle Beams, 2020, 32(10): 103002.

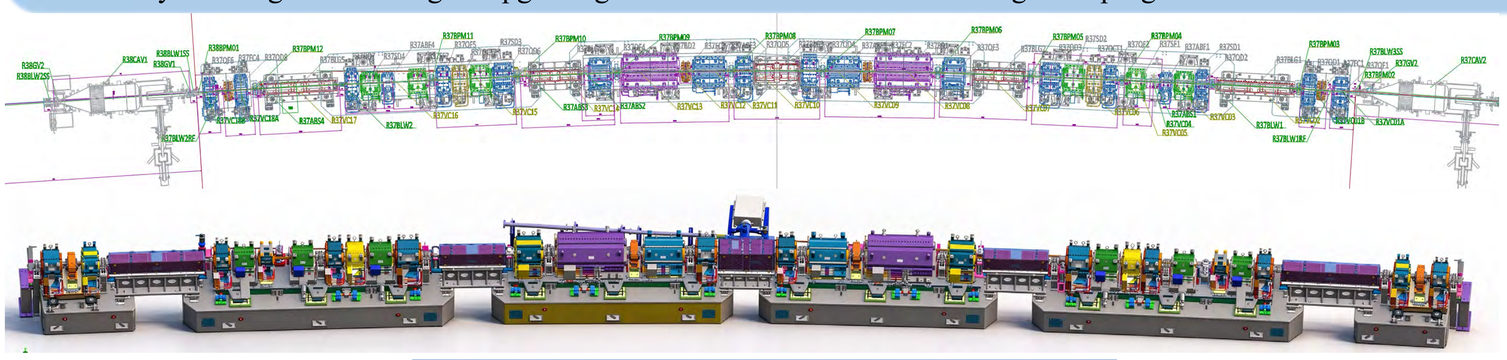
† email address: zhouzs@ihep.ac.cn

[A05]

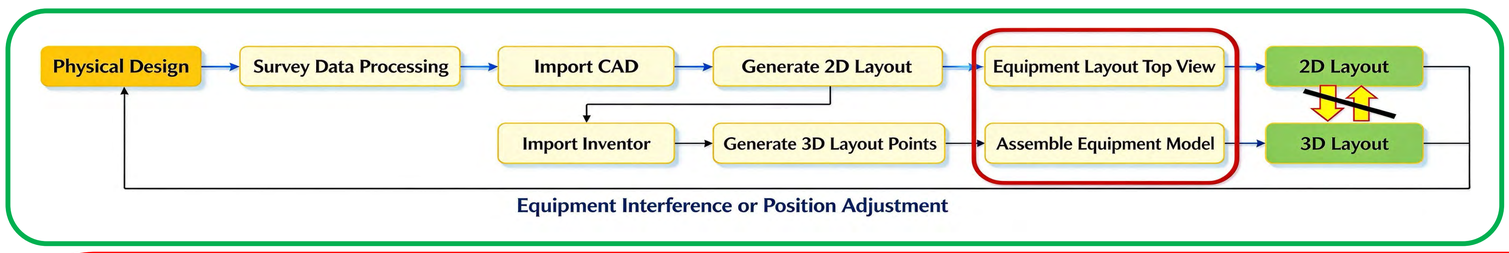
Research on 2D-3D Collaborative Layout for Particle Accelerators

Siyu Chen † , Haijing Wang
Institute of High Energy Physics, Beijing, China
† chensiyu93@ihep.ac.cn

2D and 3D layout drawings serve as core tools for the design and construction of accelerator facilities throughout their full lifecycle. With the advancement of particle and nuclear physics research, future accelerators are developing toward large-scale and ultra-precise configurations, with circumferences extending to tens or even hundreds of kilometers. Such a leap in scale leads to exponential growth in the number of equipment, which can be tens to hundreds of times that of existing accelerators, posing great challenges to preliminary layout design. For equipment layouts spanning several kilometers, manual point-by-point planning requires massive manpower for repetitive drawing and presents obvious drawbacks during model iteration. Against this backdrop, this paper proposes a 2D–3D collaborative layout mechanism, offering an innovative approach for efficient layout design and intelligent upgrading of accelerator facilities. The design and progress of this work are described herein.



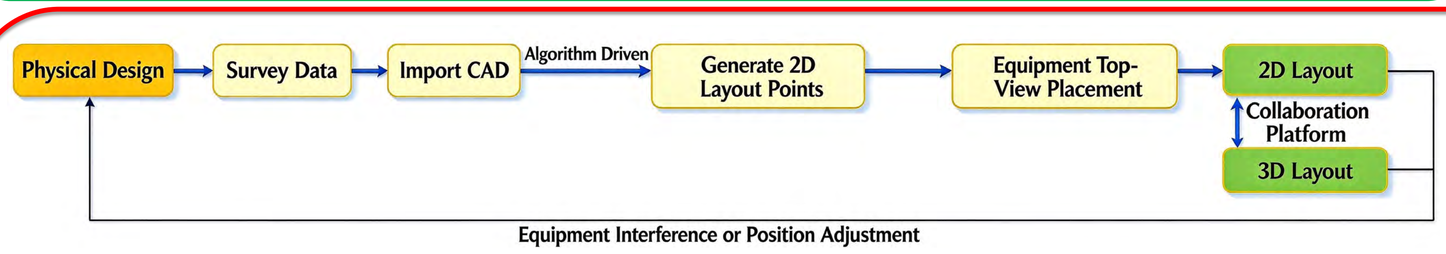
2D and 3D Layout of HEPS Storage Ring Standard Cell



At the early design stage of accelerator facilities, a phased iterative design workflow is adopted.

Nevertheless, the current design approach presents the following critical bottlenecks:

Characterized by high manual dependence, the workflow produces both layouts manually with no built-in linkage. Any modification to the physical scheme (survey data) necessitates remodelling and redrawing of both layouts, lacking automatic update capability and incurring considerable redundant work and resource consumption. Furthermore, manual drafting may introduce hard-to-detect data acquisition errors, which impose substantial risks on layout quality and equipment installation.

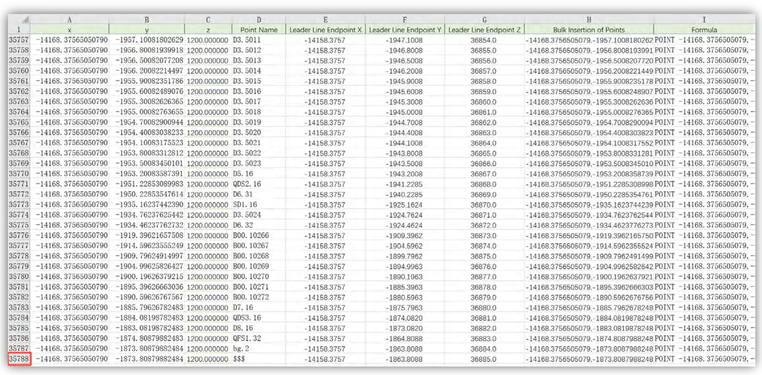




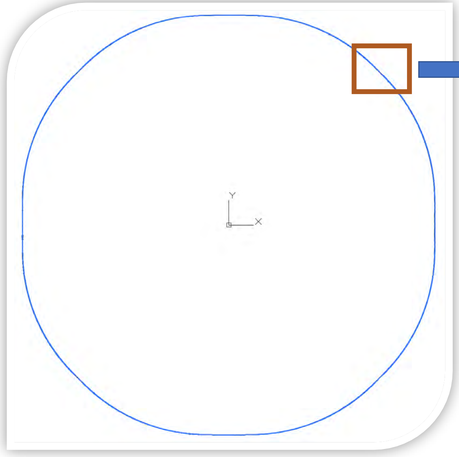
The establishment of a 2D-3D collaborative layout update mechanism breaks the bottlenecks of conventional design and eliminates the isolation between 2D and 3D layouts. It enables:

- Automatic synchronization of one layout upon modification of the other.
- Substantial reduction of manual repetitive drafting and remarkable improvement in facility layout design efficiency.
- Elimination of information discrepancy caused by delayed updates, mitigation of design conflicts and error accumulation arising from version lag, prevention of schedule delays and rising rework costs, providing technical support for efficient iteration of complex scientific facilities.

Survey Data Processing and Import



	A	B	C	D	E	F	G	H	I
1	x	y	z	Point Name	Leader Line Endpoint X	Leader Line Endpoint Y	Leader Line Endpoint Z	Bulk Insertion of Points	Formula
35757	-14168.3756505079	-1957.1008180262	1200.000000	D3.5011	-14158.3757	-1947.1008	36854.0	-14168.3756505079,-1957.1008180262 POINT	-14168.3756505079,-
35758	-14168.3756505079	-1956.8008193991	1200.000000	D3.5012	-14158.3757	-1946.8008	36855.0	-14168.3756505079,-1956.8008193991 POINT	-14168.3756505079,-
35759	-14168.3756505079	-1956.5008207728	1200.000000	D3.5013	-14158.3757	-1946.5008	36856.0	-14168.3756505079,-1956.5008207720 POINT	-14168.3756505079,-
35760	-14168.3756505079	-1956.2008221449	1200.000000	D3.5014	-14158.3757	-1946.2008	36857.0	-14168.3756505079,-1956.2008221449 POINT	-14168.3756505079,-
35761	-14168.3756505079	-1955.9008235178	1200.000000	D3.5015	-14158.3757	-1945.9008	36858.0	-14168.3756505079,-1955.9008235178 POINT	-14168.3756505079,-
35762	-14168.3756505079	-1955.6008248907	1200.000000	D3.5016	-14158.3757	-1945.6008	36859.0	-14168.3756505079,-1955.6008248907 POINT	-14168.3756505079,-
35763	-14168.3756505079	-1955.3008262636	1200.000000	D3.5017	-14158.3757	-1945.3008	36860.0	-14168.3756505079,-1955.3008262636 POINT	-14168.3756505079,-
35764	-14168.3756505079	-1955.0008276365	1200.000000	D3.5018	-14158.3757	-1945.0008	36861.0	-14168.3756505079,-1955.0008276365 POINT	-14168.3756505079,-
35765	-14168.3756505079	-1954.7008290094	1200.000000	D3.5019	-14158.3757	-1944.7008	36862.0	-14168.3756505079,-1954.7008290094 POINT	-14168.3756505079,-
35766	-14168.3756505079	-1954.4008303823	1200.000000	D3.5020	-14158.3757	-1944.4008	36863.0	-14168.3756505079,-1954.4008303823 POINT	-14168.3756505079,-
35767	-14168.3756505079	-1954.1008317552	1200.000000	D3.5021	-14158.3757	-1944.1008	36864.0	-14168.3756505079,-1954.1008317552 POINT	-14168.3756505079,-
35768	-14168.3756505079	-1953.8008331281	1200.000000	D3.5022	-14158.3757	-1943.8008	36865.0	-14168.3756505079,-1953.8008331281 POINT	-14168.3756505079,-
35769	-14168.3756505079	-1953.5008345010	1200.000000	D3.5023	-14158.3757	-1943.5008	36866.0	-14168.3756505079,-1953.5008345010 POINT	-14168.3756505079,-
35770	-14168.3756505079	-1953.2008358739	1200.000000	D5.16	-14158.3757	-1943.2008	36867.0	-14168.3756505079,-1953.2008358739 POINT	-14168.3756505079,-
35771	-14168.3756505079	-1951.2285308998	1200.000000	QDS2.16	-14158.3757	-1941.2285	36868.0	-14168.3756505079,-1951.2285308998 POINT	-14168.3756505079,-
35772	-14168.3756505079	-1950.2285354761	1200.000000	D6.31	-14158.3757	-1940.2285	36869.0	-14168.3756505079,-1950.2285354761 POINT	-14168.3756505079,-
35773	-14168.3756505079	-1935.1623744239	1200.000000	SD1.16	-14158.3757	-1925.1624	36870.0	-14168.3756505079,-1935.1623744239 POINT	-14168.3756505079,-
35774	-14168.3756505079	-1934.7623762544	1200.000000	D3.5024	-14158.3757	-1924.7624	36871.0	-14168.3756505079,-1934.7623762544 POINT	-14168.3756505079,-
35775	-14168.3756505079	-1934.4623776273	1200.000000	D6.32	-14158.3757	-1924.4624	36872.0	-14168.3756505079,-1934.4623776273 POINT	-14168.3756505079,-
35776	-14168.3756505079	-1919.3962165750	1200.000000	B00.10266	-14158.3757	-1909.3962	36873.0	-14168.3756505079,-1919.3962165750 POINT	-14168.3756505079,-
35777	-14168.3756505079	-1914.5962355524	1200.000000	B00.10267	-14158.3757	-1904.5962	36874.0	-14168.3756505079,-1914.5962355524 POINT	-14168.3756505079,-
35778	-14168.3756505079	-1909.7962491499	1200.000000	B00.10268	-14158.3757	-1899.7962	36875.0	-14168.3756505079,-1909.7962491499 POINT	-14168.3756505079,-
35779	-14168.3756505079	-1904.9962582642	1200.000000	B00.10269	-14158.3757	-1894.9963	36876.0	-14168.3756505079,-1904.9962582642 POINT	-14168.3756505079,-
35780	-14168.3756505079	-1900.1962637921	1200.000000	B00.10270	-14158.3757	-1890.1963	36877.0	-14168.3756505079,-1900.1962637921 POINT	-14168.3756505079,-
35781	-14168.3756505079	-1895.3962668303	1200.000000	B00.10271	-14158.3757	-1885.3963	36878.0	-14168.3756505079,-1895.3962668303 POINT	-14168.3756505079,-
35782	-14168.3756505079	-1890.5962676756	1200.000000	B00.10272	-14158.3757	-1880.5963	36879.0	-14168.3756505079,-1890.5962676756 POINT	-14168.3756505079,-
35783	-14168.3756505079	-1885.7962678248	1200.000000	D7.16	-14158.3757	-1875.7963	36880.0	-14168.3756505079,-1885.7962678248 POINT	-14168.3756505079,-
35784	-14168.3756505079	-1884.0819878248	1200.000000	QDS3.16	-14158.3757	-1874.0820	36881.0	-14168.3756505079,-1884.0819878248 POINT	-14168.3756505079,-
35785	-14168.3756505079	-1883.0819878248	1200.000000	D8.16	-14158.3757	-1873.0820	36882.0	-14168.3756505079,-1883.0819878248 POINT	-14168.3756505079,-
35786	-14168.3756505079	-1874.8087988248	1200.000000	QFS1.32	-14158.3757	-1864.8088	36883.0	-14168.3756505079,-1874.8087988248 POINT	-14168.3756505079,-
35787	-14168.3756505079	-1873.8087988248	1200.000000	bg.2	-14158.3757	-1863.8088	36884.0	-14168.3756505079,-1873.8087988248 POINT	-14168.3756505079,-
35788	-14168.3756505079	-1873.8087988248	1200.000000	$$$	-14158.3757	-1863.8088	36885.0	-14168.3756505079,-1873.8087988248 POINT	-14168.3756505079,-

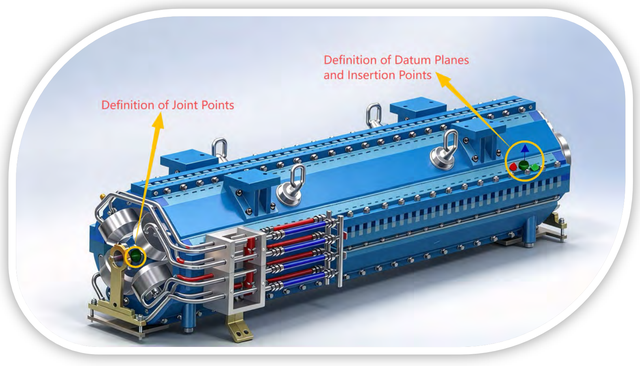




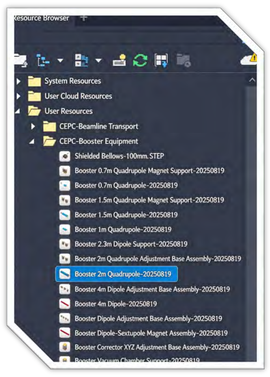
Taking the equipment layout of the CEPC Booster as an example, we first process the survey data and import it into AutoCAD via a plugin to generate a 2D point diagram containing the inlet and outlet points of each equipment.

Leader lines and corresponding point labels are automatically added to each point, so that points belonging to individual equipment can be quickly identified among thousands of points.

3D Model Processing and Asset Publishing

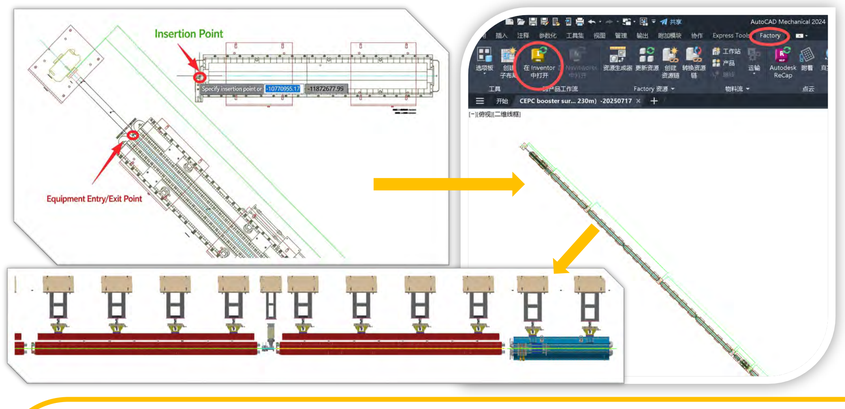






Autodesk Factory Design Utilities (FDU) is a plugin connecting Inventor and AutoCAD. It comes with built-in system resources and also supports user-defined resource libraries for factory layout creation. The FDU plugin is invoked in Inventor to process 3D models: define datum planes and insertion points, set connection points so that assets can be snapped and aligned with each other, and specify asset properties, parameters and other information. Once processing is completed, the assets can be published to the user resource library, and then viewed and retrieved from the user asset libraries in both AutoCAD and Inventor.

2D Model Processing and Asset Publishing



Assets can be retrieved in AutoCAD. Align the insertion point of each asset with the corresponding inlet/outlet point of the equipment to generate the 2D layout drawing, while the associated 3D layout drawing is created automatically. If the model is modified later and the positions of insertion points remain unchanged, one-click asset replacement can be used to fully replace the corresponding assets in both 2D and 3D layouts.

Advantages:

1.Eliminates dedicated 3D layout work and reduces workload.
2.One-click asset replacement is available after model modification or update.
3.Assets placed in AutoCAD consume fewer system resources and deliver fast performance.

Disadvantages:

1.Restricted by AutoCAD software capabilities; only 2D layout is supported at present.
2.A small number of software bugs still exist.

Future work

1. Develop an intelligent layout algorithm for equipment models. Based on survey data provided by the physical system, the algorithm can automatically place various equipment models in the 2D layout drawing and generate the 2D layout.
2. The program can automatically identify the boundary conditions for equipment installation and achieve precise positioning of equipment at designated positions according to given constraints.
3. Promote the transformation of layout design from "manual experience-driven" to "data-intelligence-driven".
4. For devices such as vacuum chambers where only the length needs adjustment while other parameters remain unchanged, Inventor iLogic is used to embed design rules into models. When design data and parameters are modified, the model updates automatically following predefined rules. This enables design automation and rapid assembly to reduce repetitive tasks.



The 2026 International Workshop on the High Energy Circular Electron Positron Collider (CEPC2026), Shanghai , China, Oct 22-26, 2026

[A06]

Multibeam Klystron Design and Development for 10 MW L-Band Operation: Simulation Results for the Electron Gun, Focusing system, RF Interaction Structure, Output Window and Collector

Noman Habib[1,2], Zu-Sheng Zhou[1,2*], Munawar Iqbal[1], Ou-Zheng Xiao[1], Yu Liu[1,2], Han Xiao[1,2] , Abid Aleem[1], Yi Ao Wang[1,2]

[1]Institute of High Energy Physics, Chinese Academy of Sciences, Beijing-China
[2]University of Chinese Academy of Sciences, Beijing-China
*Corresponding Author Email: zhouzs@ihep.ac.cn

Abstract

This paper presents the design and simulation of a 10 MW L-band (1.3 GHz) six-beam multi-beam klystron (MBK) for superconducting RF linac applications, benchmarked against the Toshiba E3736. The complete tube, comprising the electron gun with its high-voltage ceramic seal, the magnetic focusing system, the six-cavity RF interaction circuit, the output window and the collector, was designed and cross-validated with POISSON SUPERFISH, DGUN, EGUN, AJDISK, KlyC and CST Studio Suite. The six-beamlet gun delivers 134.8 A at 115 kV (0.57 μP per beam) with a cathode loading of about 2.0 A/cm², and the maximum electrode field (5.8 kV/mm) and ceramic surface fields (<1 kV/mm on the vacuum side) are well below breakdown limits. A ten-coil solenoid provides a flat axial field of 2.2 times the Brillouin field, transporting the beam with a ripple of about 5 %. The RF circuit, including one second-harmonic cavity, delivers 10.2 MW with 67 % efficiency and 48.3 dB gain in 3D PIC simulation, with 100 % beam transmission, in good agreement with KlyC 2D (10.19 MW). The WR650 pillbox window achieves S11 = −35.4 dB (VSWR = 1.034) at 1.3 GHz with a safety factor of about 14 against thermal stress. Under the full 15.5 MW DC beam, the grooved collector reaches a peak temperature of 182 °C, below the 300 °C limit. Fabrication of the tube is in progress.

Motivation

An established program in high-power RF sources for the Circular Electron Positron Collider (CEPC) injector, spanning the C-band and UHF bands, motivates the present work: an indigenous 10 MW class multi-beam klystron for superconducting RF (SRF) LINAC applications, a power class presently supplied by only three vendors worldwide Thales (TH1801), Toshiba (E3736), and CPI (VKL-8301). Developing this capability domestically shortens procurement lead times and reduces dependence on a small number of foreign suppliers for a component that is central to the injector's performance. This paper reports the first design iteration toward that goal.

Parameter	Units	Value
Frequency	GHz	1.3
Beam voltage	kV	115
Total beam current	A	134.8
Number of beamlets	------	6
Total RF output power	MW	10.2 (CST 3D PIC)
Window S11 / VSWR	dB	−35.4 / 1.034
Magnetic focusing agreement	%	~0.2 (2D vs 3D)

Table 1: MBK Parameters

Electron Gun and Beam Optics

The six-beam Pierce-type electron gun delivers six low-perveance beamlets (0.57 μP per beam, 3.44 μP total) at a cathode voltage of 115 kV, giving a total beam current of 134.8 A (22.49 A per beam) and a beam power of 15.5 MW. With a cathode diameter of 38 mm, the peak and average cathode loadings are 2.05 and 2.0 A/cm², ensuring a long cathode lifetime. The maximum electric field on the focusing electrode is 5.84 kV/mm (5.50 kV/mm in DGUN), about 26 % below the 7.9 kV/mm scaling-law limit. On the vacuum side of the HV ceramic seal the field is only 0.55–0.64 kV/mm (CST / POISSON SUPERFISH) and stays below 1 kV/mm along the whole insulator. The beam optics were cross-validated in DGUN, EGUN and CST: each beamlet converges laminarly to a 5.1 mm waist without anode interception, and in the focusing field it is transported through the 18 mm diameter drift tunnel with an average radius of 4.95–5.1 mm, a ripple of 4.0–5.0 % and a fill factor of 0.55–0.57.

Parameter	Unit	Value
Beam voltage	kV	115
Total beam current	A	134.8
Beamlets	–	6
Perveance (per beam)	μP	0.57
Cathode loading (pk/avg)	A/cm²	2.05 / 2.0
Max. E-field (optics/ceramic)	kV/mm	5.84 / 0.55
Beam radius (avg)	mm	5.1
Ripple rate	%	5.0
Fill factor	–	0.566

Table 2: Beam Optic output results

Gun and Ceramic Design

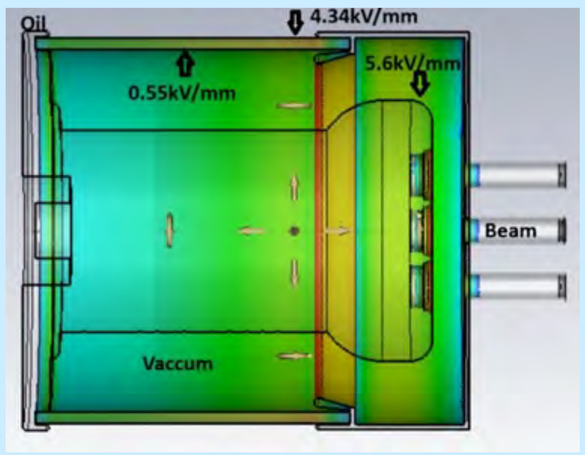


Figure 1: Electric field strength at the beam optics and HV ceramic seal of the six-beamlet gun.

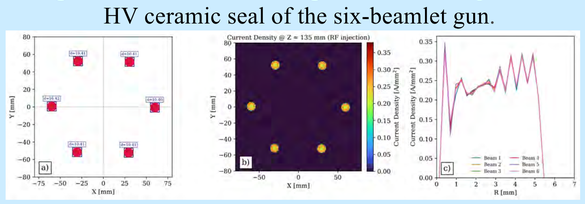


Figure 2: Six-beamlet current density map and radial current profile at the injection plane (z ≈ 135 mm).

Figure 2 describe the design results of the electron beam at the injection before entering the Rf region and its current density.

Magnet Design

We used POISSON Code to design solenoid with cathode Current Coil at the cathode for beam trajectories matching in the field free region. The design was then verified in 3D with the CST Magnetostatic Solver, including the iron yoke and six off-axis beam tunnels as shown in figure 3. The off-axis CST field overlaps the on-axis POISSON field, giving 66.6 G at the cathode, a flat top of 920 G over the RF section and a maximum of 1094 G at the collector end as shown in figure 4.

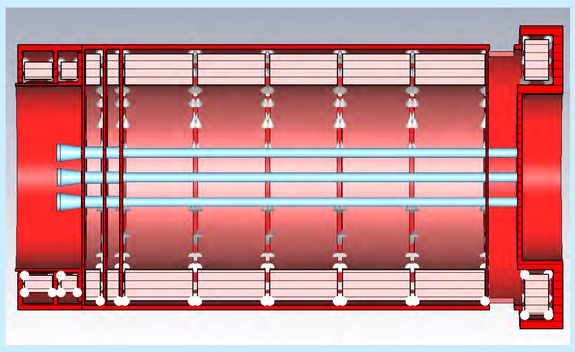


Figure 3: Magnet design in CST

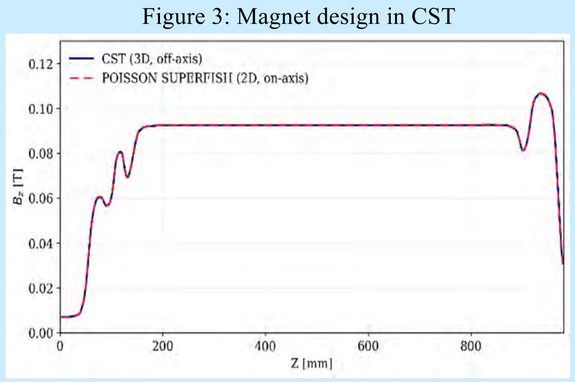


Figure 4: Magnetic field profile Comparison of the Magnet(CST&POISSON)

Magnetostatic Electron Gun

The optimized magnetic field was applied to the six-beam gun in the CST Particle Tracking Solver (Fig. 5). All six beamlets are accelerated to 115 keV and transported through their drift tunnels over the full tube length without interception. The beam reaches its equilibrium radius at z ≈ 150 mm and then keeps an edge radius of 4.84–5.29 mm, i.e. a ripple of about 5 % and a fill factor of 0.57, in good agreement with DGUN and EGUN. The RMS radius stays at 3.5–3.9 mm, showing a well-matched beam. The average radius differs by less than 5 % between the three codes.

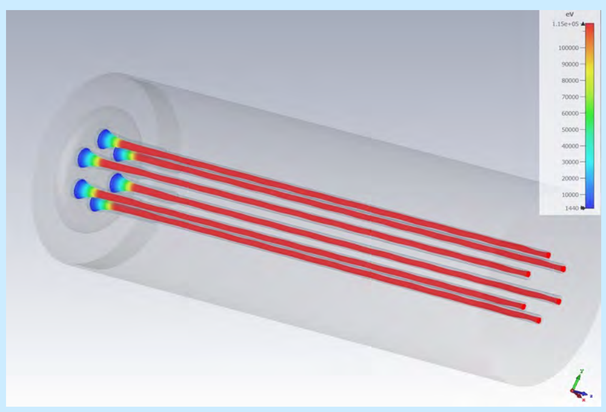


Figure 5: 3-D model of the gun produced by CST with trajectories.

RF Interaction Structure

The six-cavity RF interaction circuit, including one second-harmonic cavity (2.6 GHz), was designed to reproduce the Toshiba E3736. It was optimized with AJDISK (1D) and KlyC (2D), and the full six-beam structure was then simulated with the CST 3D PIC solver using 180 W of drive power. The beamlets enter at 115 keV, are progressively bunched along the ≈780 mm circuit and are strongly decelerated in the output cavity, with all six beams behaving identically (Fig. 6). The output signals at the two ports overlap and saturate after about 200 ns, each carrying 5.1 MW, for a total output power of 10.2 MW (Fig. 7). This corresponds to an efficiency of 67 % and a gain of 48.3 dB, with 100 % beam transmission and no reflected electrons, in good agreement with KlyC 2D (10.19 MW) and the measured E3736 (10.2 MW, 66–67 %)

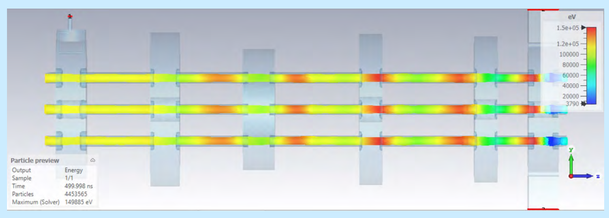


Fig. 6: CST 3D PIC simulation of the six-cavity RF circuit: electrons of the six beamlets colored by kinetic energy.

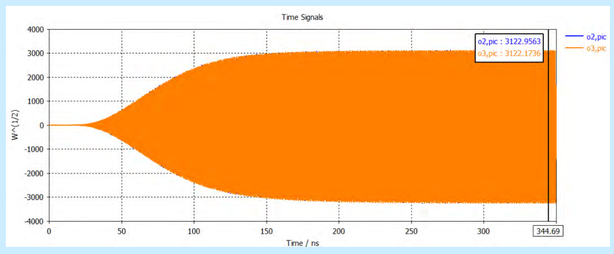


Fig. 7: Output signals at ports 2 and 3 (overlapping), giving 2 × 5.1 MW = 10.2 MW.

RF Output Window

A pillbox-type RF output window with a 99.5 % alumina disc was designed and simulated in CST, achieving a strong impedance match at 1.3 GHz: S11 = −35.4 dB and VSWR = 1.034, with a bandwidth of about 70 MHz (S11 < −20 dB). For 1 W of input power, the maximum loss density is 4.94 W/m³ on the central cross-section and 41.66 W/m³ at the edge of the ceramic disc. This loss distribution was scaled to the full average power and used in a coupled thermal structural analysis. The maximum temperature is 41.4 °C at the disc center, a temperature rise of only 16.4 °C above the 25 °C coolant. The resulting maximum von Mises stress is 21.9 MPa at the disc rim, well below the ≈300 MPa strength of alumina, giving a safety factor of about 14 as shown in Fig. 8,9,10.

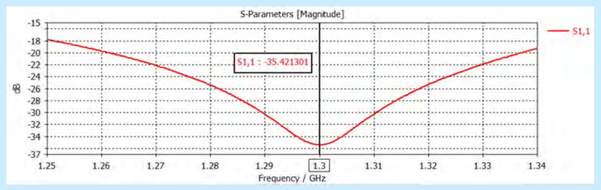


Figure 8: RF output window reflection coefficient (S11) vs. frequency.

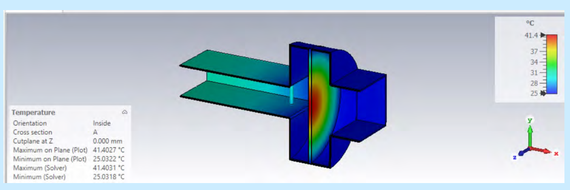


Fig. 9: Temperature distribution of the RF window

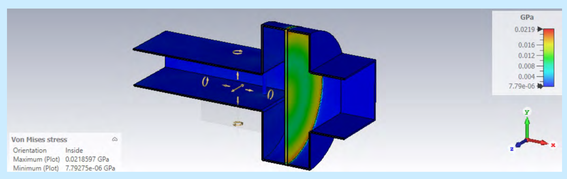


Fig. 10: Von Mises stress in the RF window

Collector

The RF circuit and the 700 mm water-cooled grooved copper collector were simulated together in CST PIC (Fig. 11). With the collector attached, the output power stays at 10.2 MW and no electrons are reflected. Under the worst case of the full 15.5 MW DC beam, the maximum collector wall temperature is 181.9 °C (Fig. 12), and integrated MBK and manufacturing progress is shown in Fig. 13 (a,b).

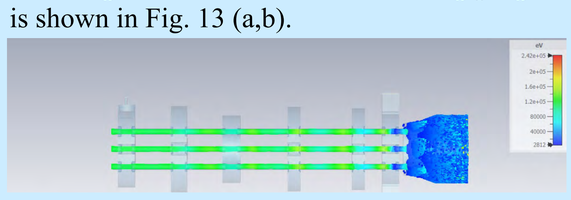


Fig. 11: RF circuit with collector (PIC)

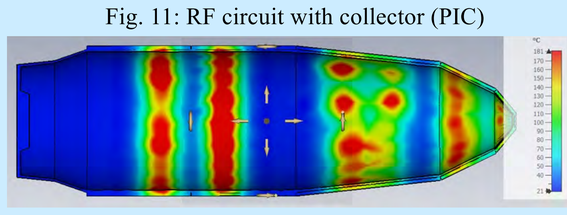


Fig. 12: Collector thermal distribution

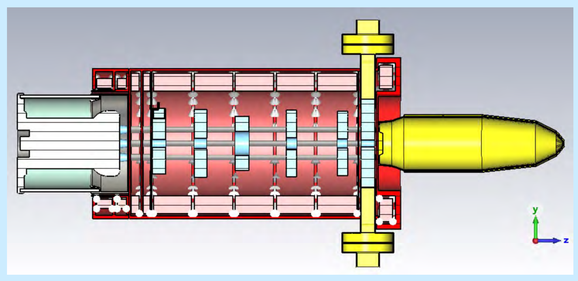


Figure 13a:Integrated design of the whole MBK in CST

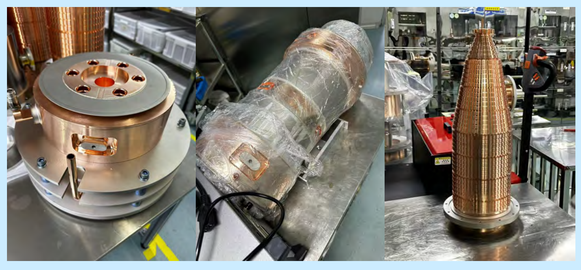


Figure 13b: shows the Manufacturing Progress of the Gun, ceramic seal, RF section and Collector.

The RF cavities, output cavity and grooved collector are machined and the RF circuit joined; gun, window assembly and high-power tests follow.

References

[1] A. Beunas and G. Faillon, "A high power long pulse high efficiency multi beam klystron," Thales Electron Devices, CERN Document Server,2001.

[2] A. Yano et al., "The Toshiba E3736 Multi-Beam Klystron," in Proc. LINAC'04, Lübeck, Germany, 2004, paper THP45.

[3] E. Wright et al., "Test results for a 10 MW, L-band multiple beam klystron for TESLA," in Proc. EPAC'04, Lucerne, Switzerland, 2004, pp. 1117–1119.

[4] **Noman Habib etl.**, CEPC study Group, CEPC Technical Design Report: Accelerator, Radiation Detection Technology and Methods, 8 (2024),1–1105.

*** Work supported by Yifang Wang's Science Studio of the Thousand Talents Project**

The 2026 International Workshop on the High Energy Circular Electron Positron Collider (CEPC2026), Shanghai, China, Oct 21-26, 2026

[A07]

中国科学院高能物理研究所
Institute of High Energy Physics, Chinese Academy of Sciences

Lattice Design and Dynamic Aperture Optimization for the BEPCII-UP with Crab Waist Scheme

Mingyang Zhao, Dou Wang, Jiuqing Wang, Yuan Zhang, Chuntao Lin
Institute of High Energy Physics, Chinese Academy of Sciences, Beijing 100049, China

Abstract

This study employs the SAD program to perform lattice design and dynamic aperture (DA) optimization for the BEPCII Upgrade Plus (BEPCII-UP) collider ring, which adopts the crab waist collision scheme. The lattice design includes the survey, optics parameters, and working point matching. To obtain a sufficient DA for injection, a combined-function magnet scheme (B+S) is explored, and a genetic algorithm (GA) is employed to optimize the strengths of the sextupoles under beam-beam interactions. The optimized lattice preliminarily meets the injection requirement, providing a reliable basis for the BEPCII-UP crab waist scheme.

Introduction

The crab waist collision scheme, featuring a large Piwinski angle, an extremely small vertical beta function (β_y^*), and dedicated crab sextupoles, is widely recognized as the preferred technology for next-generation high-luminosity electron-positron colliders. The BEPCII-UP project aims to upgrade BEPCII into a crab waist beam test facility and a $\varphi - \psi$ factory, achieving an order-of-magnitude luminosity increase in the low-energy region (≤1.89 GeV), while accumulating valuable operational experience for future colliders such as CEPC. However, the strong nonlinearities introduced by the crab sextupoles and beam-beam interactions severely limit the dynamic aperture (DA), which is crucial for injection efficiency and beam lifetime.

Overall Layout & Luminosity Goal

- A new crab waist interaction region (IR) is designed, and a superconducting wiggler (SC Wiggler) is installed in the ring to increase synchrotron radiation damping, reduce emittance, and shorten the damping time. Additionally, a compact damping ring is inserted in the middle of the Linac.

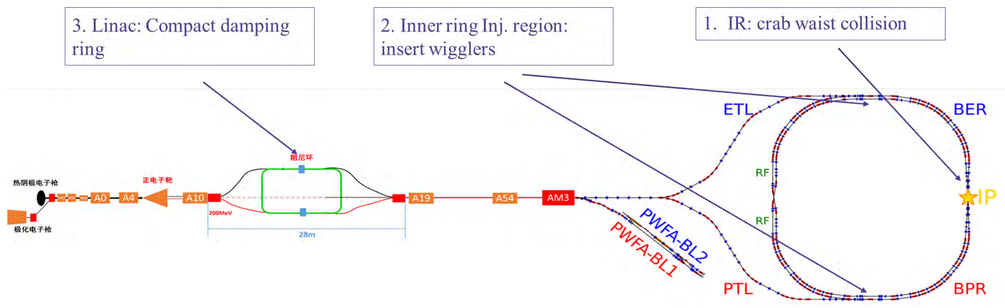


Figure 1. Overall layout of the BEPCII-UP.

- To achieve an order-of-magnitude luminosity enhancement, the target parameters at 1.89 GeV are designed: β_y^* is reduced to 5 mm, the beam-beam parameter ξ_y is increased to 0.09, and the bunch current I_b is increased to 12.5 mA.

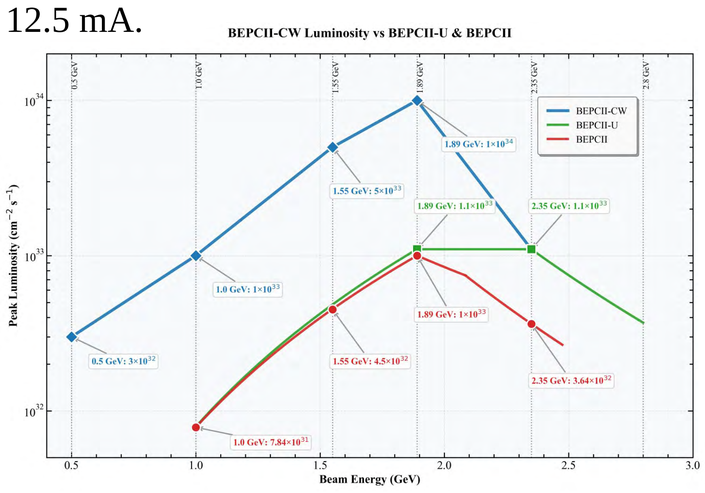


Figure 2. Luminosity performance blueprint for BEPCII-UP.

Lattice Design

- IR Geometry : Two layouts with half-crossing angles of 18.1 mrad and 40 mrad are designed. Modifications are strictly limited within ±23 m (or ±17 m) from the IP to fit the existing tunnel.

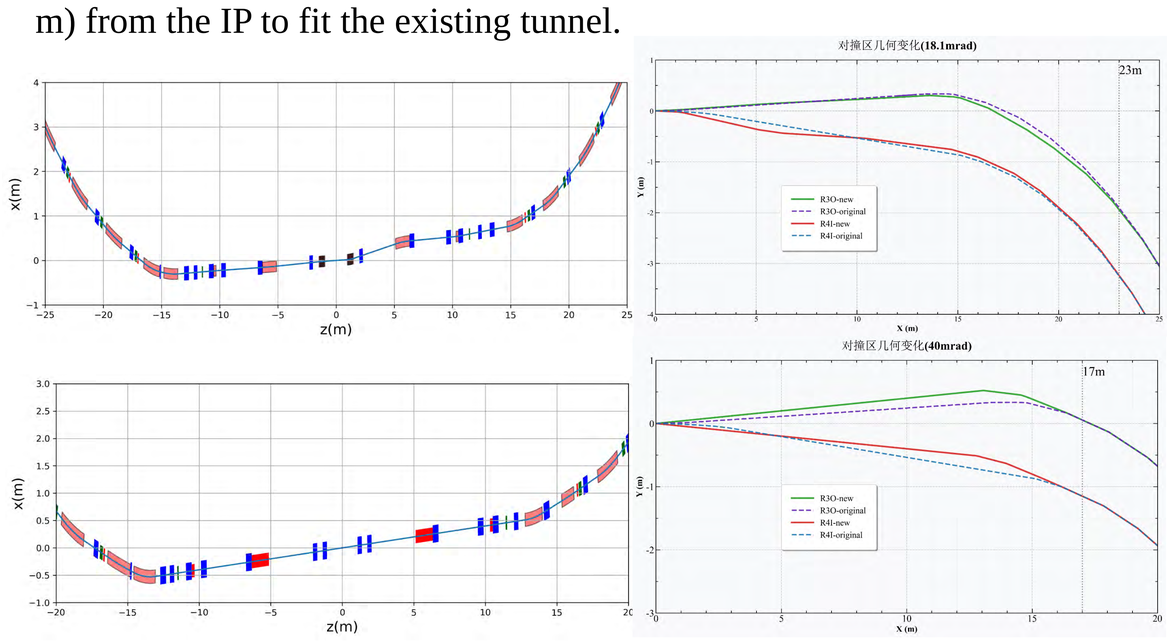


Figure 3: IR geometry for the 18.1 mrad (top) and 40 mrad (bottom) layouts.

Lattice Design

- The crab sextupoles are located at zero dispersion, and the phase advance between the crab sextupoles and the IP is set to (0.5, 0.75).

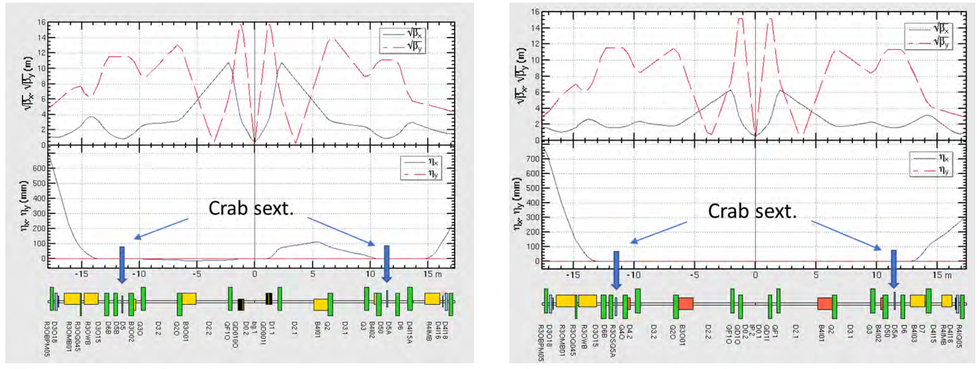


Figure 4: Optics parameter comparison near the interaction region for the 18.1 mrad (left) and 40 mrad (right).

- @0.5 GeV: A relatively large emittance is adopted to significantly improve the Touschek lifetime. This is achieved by lowering the integer part of the working point and increasing the dispersion at the wiggler section.

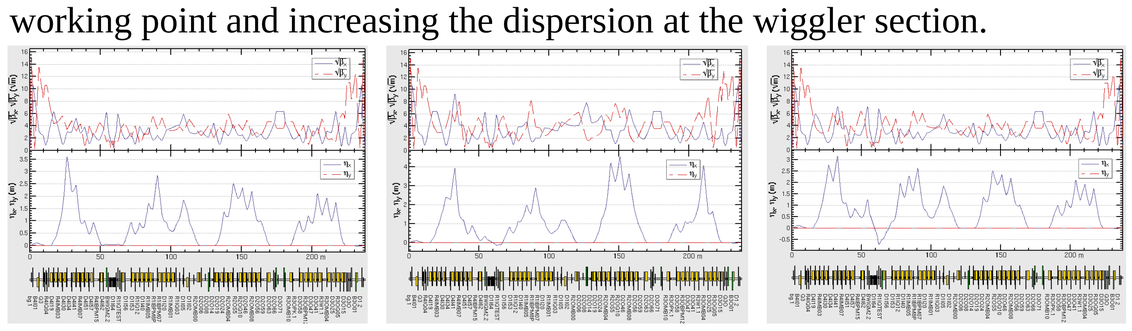


Figure 5: Three matching schemes at 0.5 GeV with emittances of 3.5 nm(left), 9 nm(middle), and 50 nm(right).

Dynamic Aperture Optimization

To enlarge the dynamic aperture, 4 new sextupoles are introduced in the IR (located between the superconducting QD/QF magnets and near the crab sextupoles). A systematic phase pairing strategy is adopted:

- Vertical Pairing: R4IS1 and R4IS5 are paired vertically, with phase advances to the final QD of π and 2π, respectively.
- Horizontal Pairing: R4IS4 and R4IS8 are paired horizontally, with phase advances to the final QF of 2π and 3π, respectively.
- The same pairing scheme is applied to the R3O region.

The best dynamic aperture (@1.89GeV) is significantly enlarged compared with the previous design. Furthermore, the number of B+S combined-function magnets is dramatically reduced from 50 to only 6. These 6 B+S magnets are distributed near the interaction region (3 in the R3O region and 3 in the R4I region), which greatly simplifies the hardware design while still maintaining a sufficient dynamic aperture for injection.

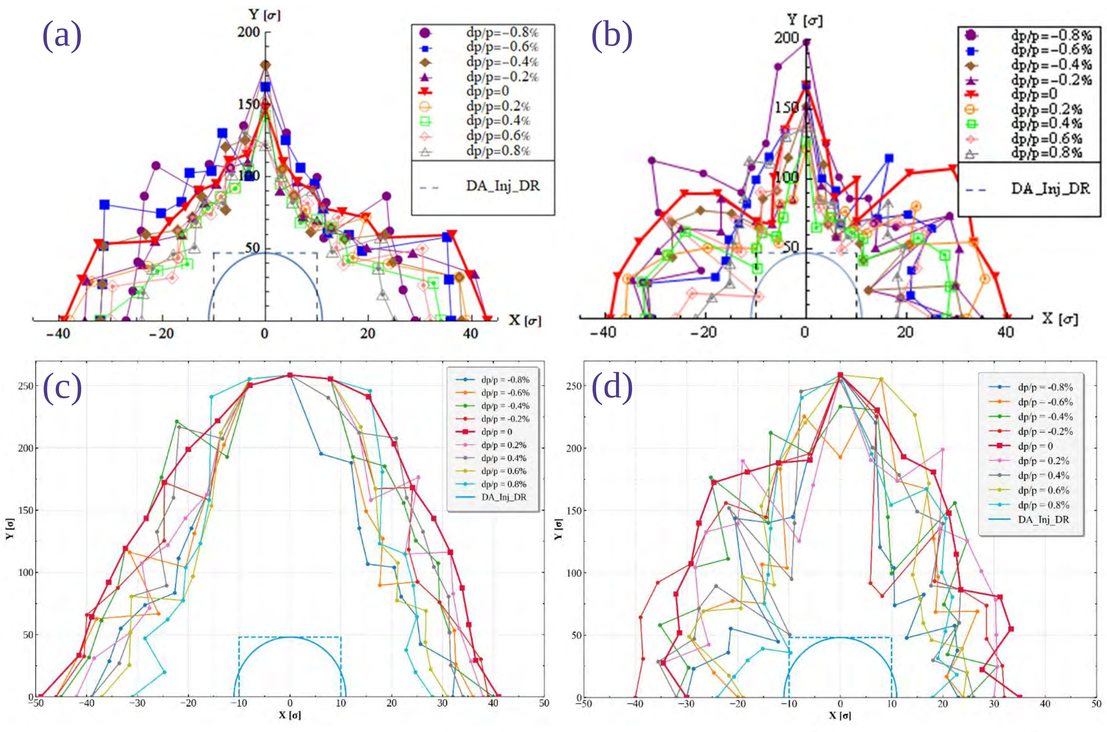


Figure 6: Dynamic aperture (DA) comparison. (a) & (b): Previous scheme consisting of the 36 original sextupoles and 50 B+S magnets, (a) W/O and (b) W/ beam-beam effects. (c) & (d): Optimized scheme containing the 36 original, 4 new sextupoles, and 6 B+S magnets, (c) W/O and (d) W/ beam-beam effects.

zhaomy@ihep.ac.cn

[A08]

The 2026 International Workshop on the High Energy Circular Electron Positron Collider (CEPC2026), Shanghai, China, Oct 22-26, 2026

Design and Optimization of High-Power, High-Efficiency S-Band Multi-Beam Klystrons for Large-Scale Scientific Facilities

S. R. Yi[1,2], Z. S. Zhou†[,1,2], O. Z. Xiao[1]

[1]Institute of High Energy Physics, Chinese Academy of Sciences, Beijing, China

[2]University of Chinese Academy of Sciences, Beijing, China

ABSTRACT

This work presents the design and analytical optimization of a high-power, high-efficiency S-band multi-beam klystron (MBK) intended as an RF power source for large-scale scientific facilities. The present design targets 2.856 GHz, 50 MW peak RF output, 62% electronic efficiency, at least 50 dB saturated gain, 3–4 μs RF pulses at 50–60 Hz, and at least 99% beam transmission. The design covers the multi-beam electron gun, magnetic focusing system, RF interaction structure, output coupling and window, and collector. The RF interaction structure combines staged fundamental bunching, harmonic correction, penultimate bunch shaping, and loaded output extraction. Drift lengths and detuning are adjusted to compress the phase distribution and maximize the fundamental beam-current component at the output gap. Output loading and magnetic focusing are subsequently matched to the bunched beam. The design is accepted only when the power, efficiency, gain, and transmission targets are achieved without excessive returning electrons, RF breakdown, or thermal loading. This approach provides a self-consistent S-band MBK design route for subsequent multi-code simulation and experimental validation.

INTRODUCTION AND DESIGN CONTEXT

The 50 MW specification refers to total peak RF output. The present 60 kV, 10 A equivalent channel provides 0.60 MW of injected beam power. Six such channels supply only 3.60 MW, below the RF target even at ideal conversion. This model supports interaction and transport development at a preliminary current level.

Related work includes the 10 MW L-band MBK for European X-FEL [1], a compact S-band MBK design [2], and a short S-band relativistic coaxial-cavity amplifier [3]. These studies guide the design approach, while differences in voltage, frequency and cavity configuration limit direct performance extrapolation.

FACTORS GOVERNING EFFICIENCY

$$\eta_e = \frac{P_{\text{out}}}{V_0 I_{\text{tot}}} \approx \frac{1}{2}\left(\frac{I_1}{I_{\text{tot}}}\right)\left(\frac{MV_g}{V_0}\right)\cos\psi$$

The efficiency relation links RF power to the fundamental beam-current component I_1, transit-time factor M, output-gap voltage and decelerating phase ψ. The denominator is the injected beam power.

Bunching raises the useful RF current component. Gap geometry controls transit-time cancellation, while cavity phase and loading determine energy extraction. Magnetic focusing must retain the beam through the interaction gaps as the particles decelerate.

RF CHAIN AND FOCUSING

Six cavities form the RF chain. C4 supplies second-harmonic correction and C5 shapes the bunch before output extraction.

The output cavity has cold $f_0 = 2855.997$ MHz, $(R/Q)_{\text{cell}} = 125.010\ \Omega$, $Q_0 = 6086.5$ and $Q_L = 52$.

Injection uses a 1.2 mm radius and zero initial slope. The prescribed downstream field is about 2700 G, with cathode $B_{\text{zc}} = 64.952$ G. Transport and RF matching remain coupled optimization variables.

MODEL AND RF EVOLUTION

The 2D EMSYS model uses 60 kV and 10 A per equivalent channel, with a 1.2 kW drive at 2.856 GHz. The 220-cycle run uses mesh steps $\Delta r = 0.20$ mm and $\Delta z = 0.25$ mm.

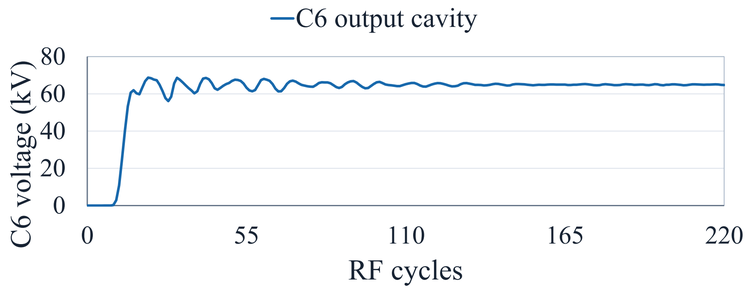


Fig. 1. Archived output-cavity voltage. The final value is 64.73 kV, with a last-20-cycle range of 64.63–65.15 kV.

BEAM DYNAMICS

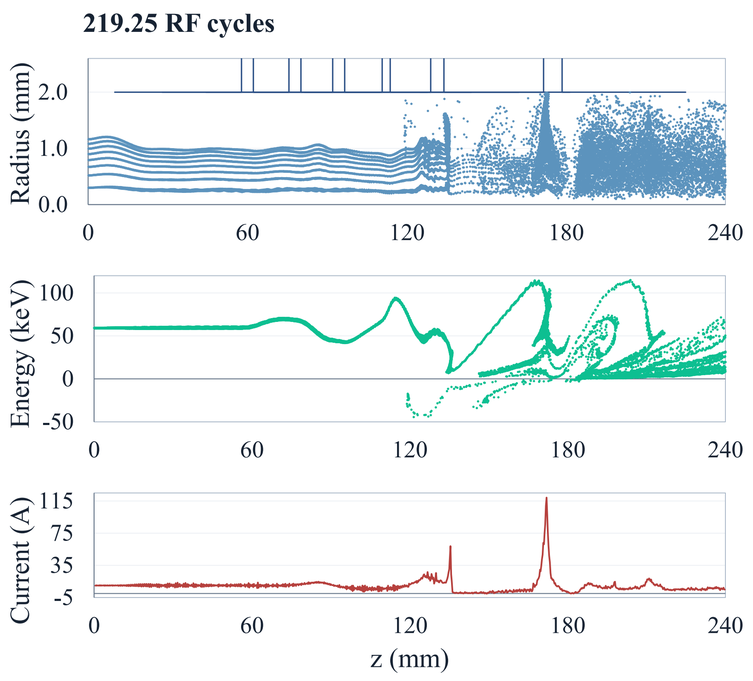


Fig. 2. Selected snapshot at 219.25 RF cycles: radius, native signed energy and current. The output-gap current peak is the strongest of the four archived phases.

The peak $I_{\text{z,pk}} = 119.26$ A is at $z = 172$ mm, within the output gap. The injected DC current is $I_0 = 10$ A.

The downstream energy and radial spread identify focusing during deceleration as a remaining optimization priority.

CURRENT MODEL: FINDINGS

The archived run gives approximately 322 kW RF output from 600 kW of injected beam power per equivalent channel.

The output-cavity voltage builds up and its oscillation amplitude decreases. Over the final 20 cycles, its coefficient of variation is 0.245%. This indicates limited voltage fluctuation within the recorded window. Longer runs and mesh refinement are still needed to assess numerical convergence.

The selected beam snapshot illustrates local bunching. It alone cannot establish current transmission or time-averaged efficiency.

EFFICIENCY AND TRANSPORT LIMITS

The drift-wall and output-cavity-wall diagnostics report 14.356% and 9.505% beam-energy loss. Focusing during deceleration must accommodate the changing energy spread while retaining the beam and preserving useful bunch compression.

The 30.246% dump residual motivates scans of output tuning, loading and decelerating phase. Greater extraction must avoid excessive slowing, reflection and interception. These diagnostics exclude RF ohmic heating and do not form a verified closed budget. Longer runs, finer meshes and particle-count checks should establish the sensitivity of losses and RF conversion.

DEVELOPMENT TOWARD 50 MW

At the 62% efficiency target, 50 MW requires 80.65 MW of peak beam power, or about 224 A per beam at 60 kV with six beams. This is 22.4 times the present current and requires feasibility validation.

Development starts with gun design and matched transport, followed by joint RF and focusing optimization under stronger space charge. Direct external-coupling scans and 3D multibeam simulations must assess loading and field asymmetry. Pulse heating, window limits and collector loading require separate evaluation. The present efficiency cannot be extrapolated without convergence, transmission and power-balance checks at the required current.

REFERENCES

[1] Y. H. Chin et al. Development of 10 MW L-Band Multi-Beam Klystron (MBK) for European X-FEL Project. Proceedings of PAC07, WEPMN023, pp. 2098–2100, 2007. https://proceedings.jacow.org/p07/PAPERS/WEPMN023.PDF

[2] X. Lin et al. Design and simulation of an S-band compact multi-beam klystron. AIP Advances, 13, 115023, 2023. https://doi.org/10.1063/5.0157492

[3] L. Sun et al. Short-Length, High-Efficiency S-Band Coaxial Cavity Relativistic Multibeam Klystron Amplifier for Potential High Power Microwave Application. IEEE Electron Device Letters, 43(10), 1760–1763, 2022. https://doi.org/10.1109/LED.2022.3200689

[4] O.-Z. Xiao et al. Design and high-power test of 800-kW UHF klystron for CEPC. Chinese Physics B, 31, 088401, 2022. https://doi.org/10.1088/1674-1056/ac6b26

[5] J. Plouin et al. Design, Fabrication, and Test of a 5 GHz Klystron Based on the Kladistron Principle. IEEE Transactions on Electron Devices, 70(3), 1275–1282, 2023. https://doi.org/10.1109/TED.2023.3236590 https://arxiv.org/html/2404.05493v1

[6] Z. Liu, H. Zha, J. Shi, H. Chen. Design of the HOM MBK With Multiple-Gap Output Cavity. IEEE Transactions on Electron Devices, 69(2), 741–747, 2022. https://doi.org/10.1109/TED.2021.3134595

*** Work supported by Yifang Wang's Science Studio of the Thousand Talents Project and National Key Programme for ST Research and Development (Grant No. 2024YFA1610602).** **† zhouzs@ihep.ac.cn**

The 2024 International Workshop on the High Energy Circular Electron Positron Collider (CEPC2024), Shanghai, China, Oct 22-26, 2024

[A09]

*Electric Field Gradient Optimization and Multi-Dimensional Performance Verification of an S-band 80 MW Klystron Electron Gun Based on NSGA-II Algorithm**

Yuying Ding[1,2], Zusheng Zhou[†1,2], Ouzheng Xiao[1]

1. Institute of High Energy Physics, Chinese Academy of Sciences, Beijing 100049, China

2. University of Chinese Academy of Sciences, Beijing 100049, China

The operating voltage of high-power klystron electron guns reaches the hundred-kilovolt level. High electric-field gradient inside the gun readily causes vacuum breakdown and other adverse phenomena, which degrade the voltage withstand capability and service life of the device. Taking a high-efficiency klystron electron gun as the research object, this paper adopts the Non-dominated Sorting Genetic Algorithm-II (NSGA-II) multi-objective genetic algorithm to collaboratively optimize the geometric dimensions of the focusing electrode for electric-field gradient suppression. Two optimized configurations with different fillet radii for the focusing electrodes are obtained. Subsequently, steady-state temperature field, thermal deformation and modal oscillation verification are carried out simultaneously. The eigenmodes of the optimized structure are far away from the operating excitation frequency band, and no risk of self-excited oscillation exists. This research provides a theoretical basis for the low-electric-field structural design of similar high-power klystron electron guns.

Background

The electron gun operates under prolonged high-voltage conditions, and excessive electric field gradients can easily lead to breakdown, causing significant field emission and potentially triggering secondary electron emission effects. This not only results in voltage collapse or pulse truncation but may also cause surface ablation due to energy deposition, further deteriorating surface roughness and continuously lowering the subsequent electrical breakdown threshold, thus forming a vicious cycle. Optimizing the electrode structure of the electron gun's beam optics enables control over the amplitude and spatial distribution of the cavity's electric field at the source, representing a key technical approach to improving klystron efficiency and long-term operational reliability. In this study, the NSGA-II multi-objective optimization algorithm was employed to perform coordinated optimization of the geometric parameters of an electron gun in a specific klystron. The optimization effectively suppresses peak electric field gradients within the gun and broadens its stable high-voltage operating range, achieving enhanced voltage withstand capability without significantly increasing material or manufacturing costs. This work provides theoretical guidance and design insights for structural development and iterative improvement of similar high-power klystron electron guns.

Electron Gun Theory Model and Design Foundation

The beam optical design of the fast-traveling tube electron gun is based on the Pierce theory. This report selects the design parameters of a certain high-power fast-traveling tube as the design target. The design parameters are shown in Table 1.

Table 1 klystron design parameters

parameters	value
Beam voltage	350 kV
Beam perveance	2 μP
Radius ratio of electron beam tube b/a	0.7

After calculation based on the Pierce theory, the cathode and anode parameters obtained are consistent with the parameters of the prototype electron gun. The original focusing electrode with the maximum electric field gradient exceeding 26 kV/mm had a potential risk of vacuum breakdown. Compared with the process improvement scheme of replacing the focusing electrode with stainless steel material, the optimization idea of adjusting the geometric parameters of the focusing electrode to achieve electric field suppression can significantly reduce the processing cost and physical experiment cost of the device, and is the core optimization scheme adopted in this study. As shown in Figure 1, first, the actual structural characteristics of the electron gun focusing electrode were parameterized, and then a coordinate system was established to represent the geometric relationship of each parameter to adapt to the setting of the optimization program parameters.

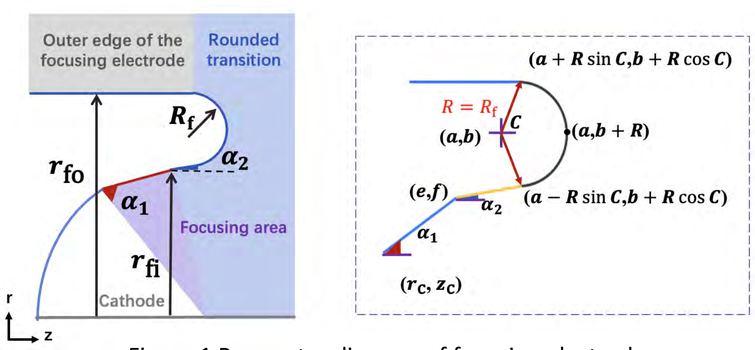


Figure 1 Parameter diagram of focusing electrode

Optimization of Electron Gun Surface Electric Field Based on NSGA-II

NSGA-II (Non-dominated Sorting Genetic Algorithm II) optimization is a method that continuously iteratively selects better solutions within the population through a process similar to biological genetics. In this paper, the DGUN two-dimensional calculation software is called in the optimization program for the beam optics calculation of the electron gun, and the output results are used as the evaluation basis. The optimization logic of the program is shown in Figure 2, and the optimization iteration process is shown in Figure 3.

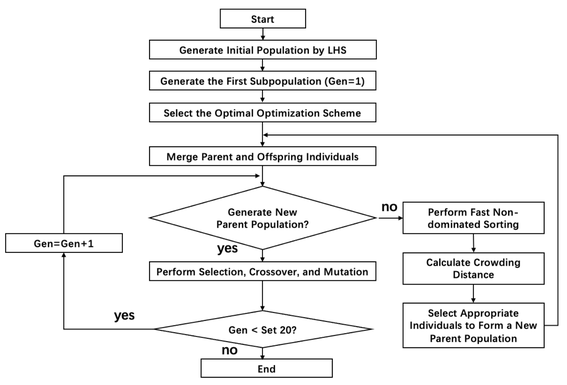


Figure 2 program flow chart

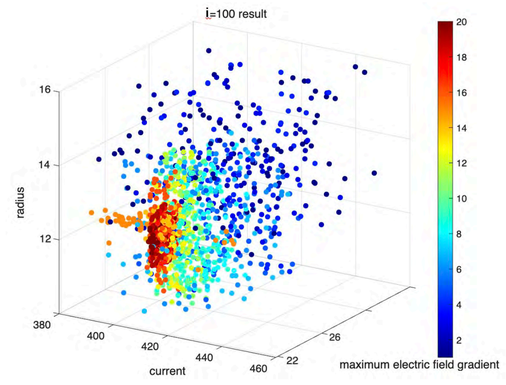


Figure 3 Program results

Initially, two sets of configuration schemes with small and large extreme circular arc radii were selected for comparative analysis, as shown in Figure 4. An attempt was made to focus the beam using the focused magnetic field generated by the original coil. The two schemes were compared with the original beam. The results showed that the optical properties of the optimized electron gun beam were nearly the same as the original.

The maximum electric field gradients obtained from the two optimization schemes in the two-dimensional and three-dimensional beam optics beam current calculation simulations were both lower than that of the prototype electron gun (26 kV/mm). This further confirmed the validity and reliability of the output results of the multi-objective optimization algorithm. Subsequently, scheme one with a lower electric field gradient was selected as the final optimization scheme for subsequent verification calculations.

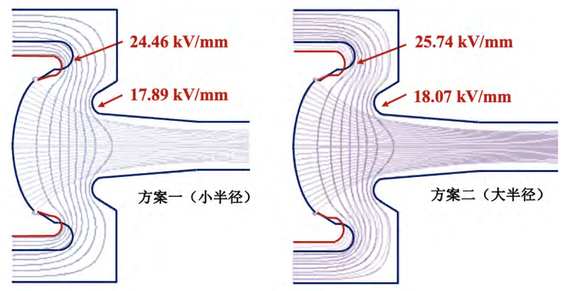


Figure 4 Scheme one and scheme two are compared with the original electron beam optical system in DGUN

Thermal Characteristics

When the speed-modulation tube electron gun is operating, the cathode temperature can reach 1050°C. The heating of the cathode and the focusing electrode causes optical changes in the beam, and it is necessary to reserve space for thermal deformation in advance through thermal characteristic analysis.

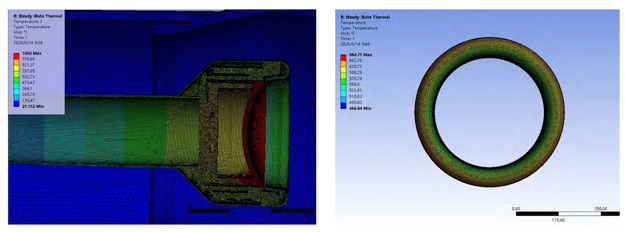


Figure 5 Thermal Characteristic results in ANSYS

Self-excited Oscillation Verification

The self-excited oscillation of the gun model mainly stems from the energy exchange between the electron beam and the high-frequency structure in the electron gun area. By constructing the internal geometric model of the gun area and using the CST calculation software, the quality factor Q_{total} of the electron gun can be obtained.

$$\frac{1}{Q_{\text{total}}} = \frac{1}{Q_0} + \frac{1}{Q_{\text{ext}}} + \frac{1}{Q_e}$$

The calculation results to the intrinsic mode of the electron gun area show that $Q_{\text{total}} > 0$, indicating that the electron gun has no self-excited oscillation mode. The remaining structures do not need to be modified to prevent the gun model from oscillating, and the overall optimization and verification of the electron gun are completed simultaneously.

Summary and Outlook

Taking a certain actual high-power speed-modulator electron gun as the research object, the Pierce electron gun focusing electrode was optimized by using the NSGA-II algorithm for the coordinated optimization of multiple geometric parameters. Combined with multi-field simulation, multiple performance verifications were completed. In the future, the working voltage will be increased in actual engineering applications such as processing and testing, and the optimization results will be further verified.

*** Work supported by Dr. Yifang Wang's Science Studio of the Thousand Talents Project**

† email address: zhouzs@ihep.ac.cn

The 2026 International Workshop on the High Energy Circular Electron Positron Collider (CEPC2026), Shanghai, China, Oct. 22–26, 2026

[A10]

Design of an S-Band 50 MW Periodic Permanent Magnet Focused Klystron†

Han Xiao[1,2], Zusheng Zhou[1,2,*], Ouzheng Xiao[1], Yu Liu[1,2], Yiao Wang[1,2], Munawar Iqbal[1], Abid Aleem[1]

[1] Institute of High Energy Physics, Chinese Academy of Sciences, Beijing 100049, China
[2] University of Chinese Academy of Sciences, Beijing 100049, China
*email address: zhouzs@ihep.ac.cn

ABSTRACT

Improving klystron efficiency is essential for reducing the operational cost of particle accelerators. This work presents the physical design of an S-band 50 MW high-efficiency klystron with periodic permanent magnet (PPM) focusing, which eliminates the power consumption of electromagnetic focusing coils. A low-perveance beam of 1.3 μP and two second-harmonic bunching cavities are adopted to enhance the bunching, and a segmented PPM structure balances the beam rigidity with the cavity dimensions. Three-dimensional particle-in-cell (PIC) simulations give an output power of 51.2 MW and an efficiency of 53.8%, with no reflected electrons. The overall tube length is 1310 mm.

INTRODUCTION

Klystrons are vacuum electronic devices that convert electron-beam energy into microwave power through velocity modulation, featuring high power, high gain, and high efficiency. Improving klystron efficiency directly reduces the operational cost of particle accelerators. For low-duty-factor klystrons in linacs, the power consumption of electromagnetic focusing coils is not negligible: the conversion efficiency of the BEPC linac klystrons in operation is 41.3%–48.3%, but drops to 34%–43% when coil losses are included. Worldwide, the efficiency of S-band 50 MW klystrons is around 43%, so the overall efficiency including coil losses is below 40%.

Permanent magnet focusing removes the coil power supplies and cooling systems, saving about 15% of the cost. KEK and SLAC have developed PPM klystrons with efficiencies of 48% at C-band (5712 MHz, 50 MW) [1] and 50%–55% at X-band (11424 MHz, 50–75 MW) [2, 3].

PERIODIC PERMANENT MAGNET FOCUSING

Reverse leakage fields exist on both sides of a single axially magnetized ring. With alternating polarity, the fields of adjacent rings reinforce each other to form a periodic focusing field (Figure 1) [3]. A low-perveance beam and second-harmonic bunching cavities are adopted to enhance the bunching efficiency.

RESEARCH OBJECTIVES

The design goals are listed in Table 1.

Parameter	Value
Operating frequency (MHz)	2856
Output power (MW)	≥50
Efficiency (%)	≥53
Focusing structure	PPM
Pulse width (μs)	4
Repetition rate (Hz)	50

Table 1 Design goals

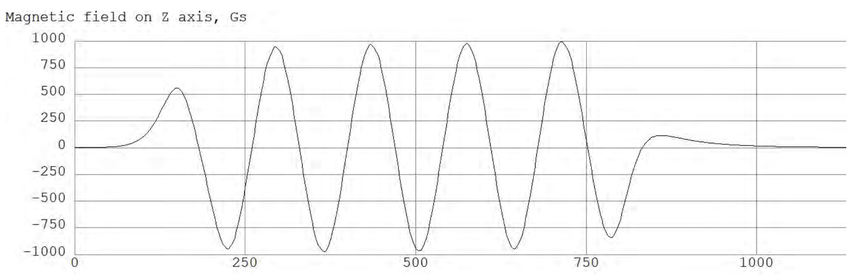


Figure 1 Periodic field of alternating magnet rings

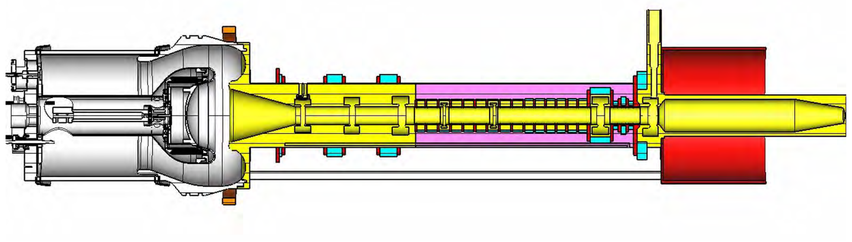


Figure 2 Overall structure of the klystron (1310 mm)

BASIC DESIGN

An operating beam of 350 kV and 272 A (1.3 μP) was selected. The drift-tube radius is 13.8 mm to accommodate the second-harmonic cavities. With a 0.65 fill factor, the beam radius is 9 mm, the area compression ratio is 27, and the Brillouin field is 625 Gs.

Parameter	Value
Beam voltage (kV)	350
Beam current (A)	272
Perveance (μP)	1.3
Drift tube radius (mm)	13.8
Beam radius (mm)	9
Fill factor	0.65
Area compression ratio	27
Brillouin field (Gs)	625

Table 2 Main beam parameters

ELECTRON OPTICS

The electron gun follows an existing cathode–focusing-electrode design. Extending the cathode–anode gap sets the current to 272 A; increasing the anode-tip radius gives a waist radius of 8.6 mm. The maximum surface field is 22.3 kV/mm.

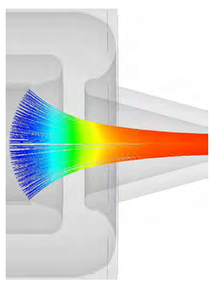


Figure 3 Electron trajectories of the gun

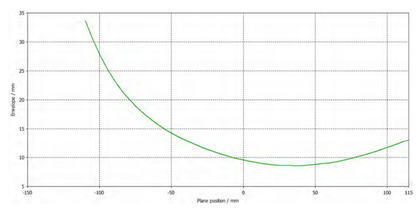


Figure 4 Beam envelope in the gun region

MAGNETIC FOCUSING STRUCTURE

A segmented PPM structure is adopted. The magnetic half-period decreases in steps from 84 to 12 mm while the on-axis field rises to 1630 Gs. Above the low-voltage stop-band [3], beam transmission rises sharply near 20 kV and reaches 99.8% at 70 kV (Figure 6).

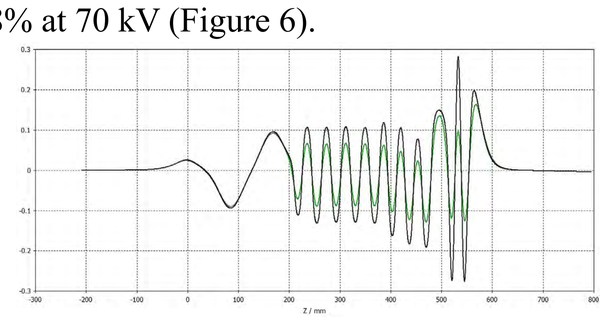


Figure 5 Magnetic field on the axis and at the beam edge

RF CIRCUIT DESIGN

Re-entrant cavities keep higher-order modes away from beam harmonics. Cavities 1–3 are stagger-tuned for bandwidth; cavities 4 and 5 operate at the second harmonic to bunch core and outer electrons. The output-cavity frequency is tuned to the beam energy–phase distribution. Parameters are listed in Table 3.

Cavity	Qe	f (MHz)
1	179	2852
2	—	2860
3	—	2868
4	—	5678.4
5	—	5638.3
6	—	2946.9
7	32.8	2832

Table 3 Cavity parameters

BEAM DYNAMICS

The one-dimensional model predicts 64.8% efficiency; three-dimensional PIC simulations in CST [4] were therefore used for the final optimization. The second-harmonic cavities and output cavity were tuned using the electron phase space. Figures 7 and 8 show the longitudinal phase space and transverse trajectories, respectively. The output reaches 51.2 MW at 53.8% efficiency, with no reflected electrons.

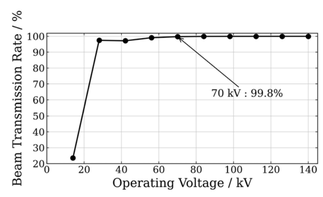


Figure 6 Beam transmission vs voltage

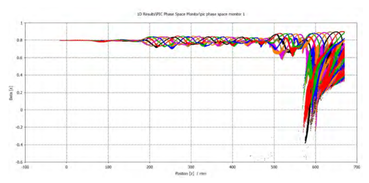


Figure 7 Longitudinal phase space (z–βz)

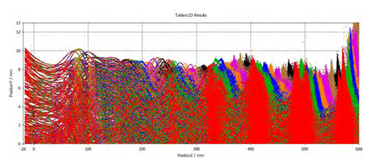


Figure 8 Transverse trajectories (y–z)

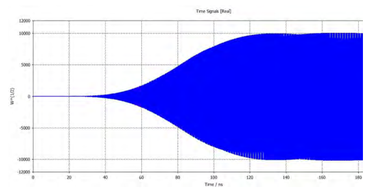


Figure 9 Output signal (3D PIC)

SUMMARY AND OUTLOOK

PPM focusing eliminates the coil power supplies and cooling systems, resulting in a compact tube length of 1310 mm. Two second-harmonic cavities strengthen the electron bunching, while the segmented PPM structure balances the beam rigidity with the cavity dimensions. Three-dimensional PIC simulations [4] give an output power of 51.2 MW at 53.8% efficiency with no reflected electrons, and the beam transmission reaches 99.8% at 70 kV. Prototype fabrication and high-power testing will follow.

REFERENCES

[1] H. Matsumoto et al., “High power test of the first C-band (5712 MHz) 50 MW PPM klystron,” Proc. PAC 2001, vol. 2, pp. 993–995, 2001.
[2] Y. H. Chin et al., “X-band PPM klystron development for JLC,” Proc. PAC 2001, vol. 5, pp. 3792–3794, 2001.
[3] D. W. Sprehn et al., “Periodic permanent magnet development for linear collider X-band klystrons,” SLAC-PUB-7928, 1998.
[4] CST Studio Suite, Dassault Systèmes, Darmstadt, Germany.

†Work supported by Yifang Wang’s Science Studio of the Thousand Talents Project and National Key Programme for ST Research and Development (Grant NO.: 2024YFA1610602)

CEPC 2026 [A11]

Institute of High Energy Physics
Chinese Academy of Sciences

Numerical and Experimental Investigation of Cooling-Water-Induced Excitation and Structural Response for Accelerator Magnet Applications

Yuqi Zhang[1,2], Zihao Wang[1], Chunhua Li[1], Huamin Qu[1]

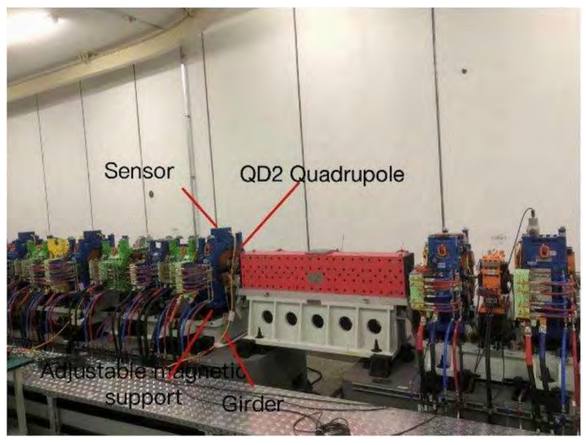
[1] Institute of High Energy Physics, Chinese Academy of Sciences, Beijing, China
[2] University of Chinese Academy of Sciences, Beijing, China

1 Abstract and Motivation

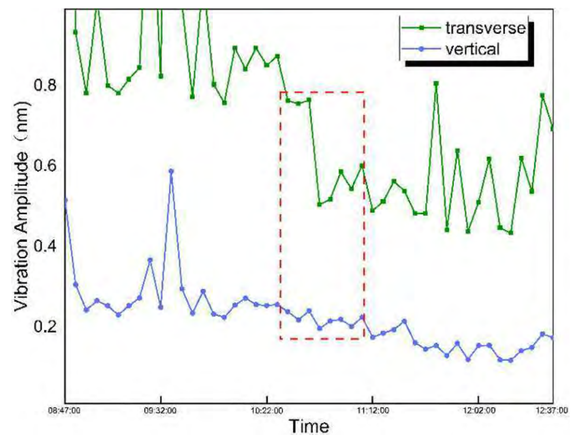
ABSTRACT

The stringent vibration requirements of the Circular Electron Positron Collider (CEPC) make mechanical stability an important design consideration. CEPC studies specify RMS ground-motion requirements over 1-100 Hz of ≤4 nm for the machine-detector interface (MDI) and ≤24 nm for the collider arc, straight and radio-frequency sections [1]. Alongside ground-transmitted vibration, cooling-water operation may also affect magnet vibration. Measurements on the HEPS QD2 magnet show a decrease in transverse displacement RMS after cooling-water shutdown [2], motivating investigation of the associated excitation and response.

This study uses large-eddy simulation to investigate fluid excitation in a simplified 90° bend and laser vibrometry to examine vibration on a bent-pipe rig. The simulations reveal spatial variations in wall-pressure fluctuations, while the measurements show increased pipe vibration over 100-800 Hz during pump operation. These findings provide a basis for future work linking fluid loads to structural response through modelling and experimental validation.

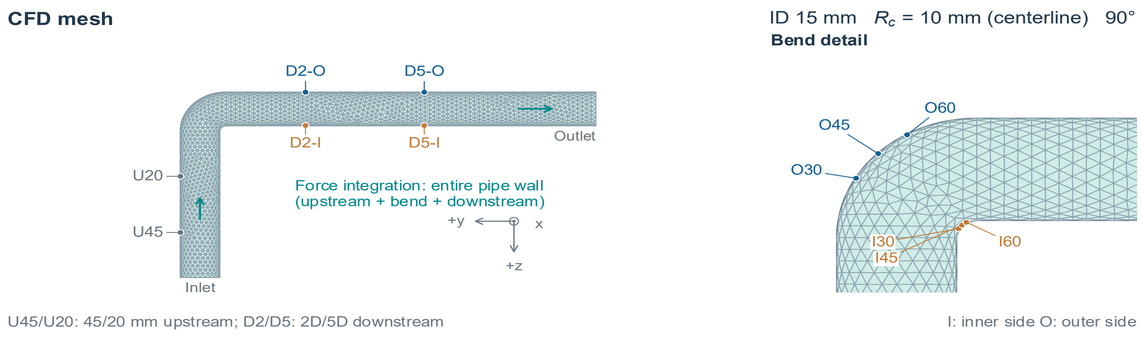


HEPS QD2 Magnet and Vibration Measurement [2]

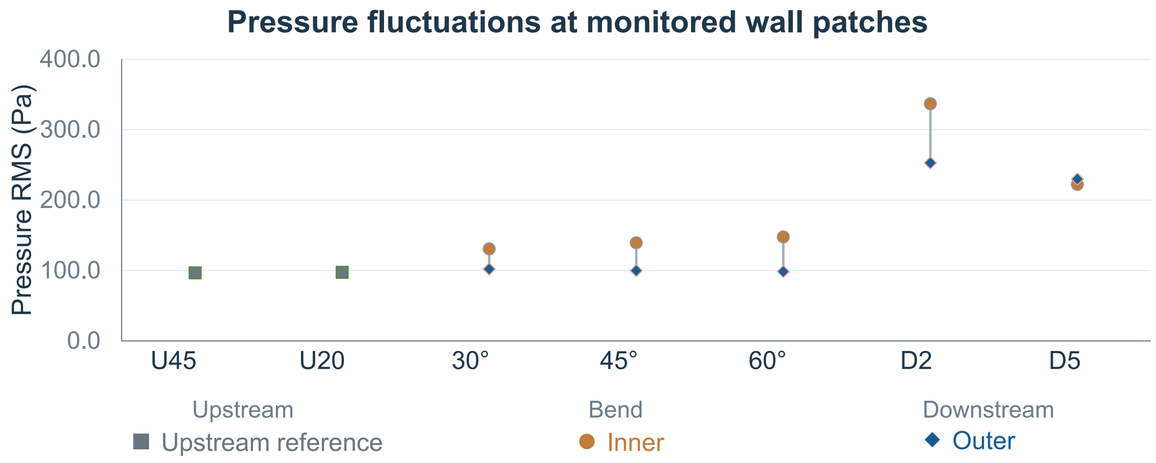


Displacement RMS (1-100 Hz). Red box: reduced transverse vibration after water shutdown [2].

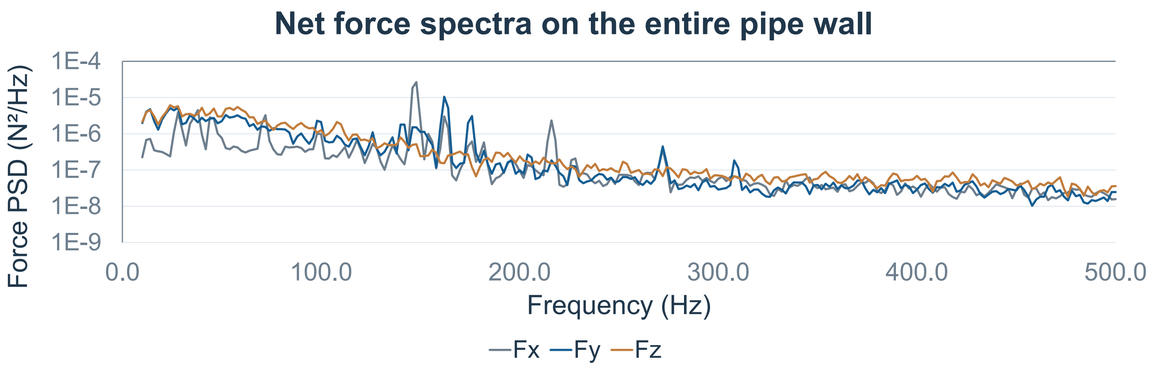
2 Flow Excitation



A 90° bend (ID = 15 mm, centreline radius R = 10 mm) is simulated using WALE LES with an STG inlet at 2.3 m/s. The mesh contains 114,106 cells; Δt = 50 μs.



The highest monitored RMS occurs at D2-I (337 Pa), compared with 97 Pa at U45. Inner-outer differences decrease between D2 and D5. Values are RMS fluctuations of patch-averaged pressure. Thin lines connect paired inner and outer values at the same station.

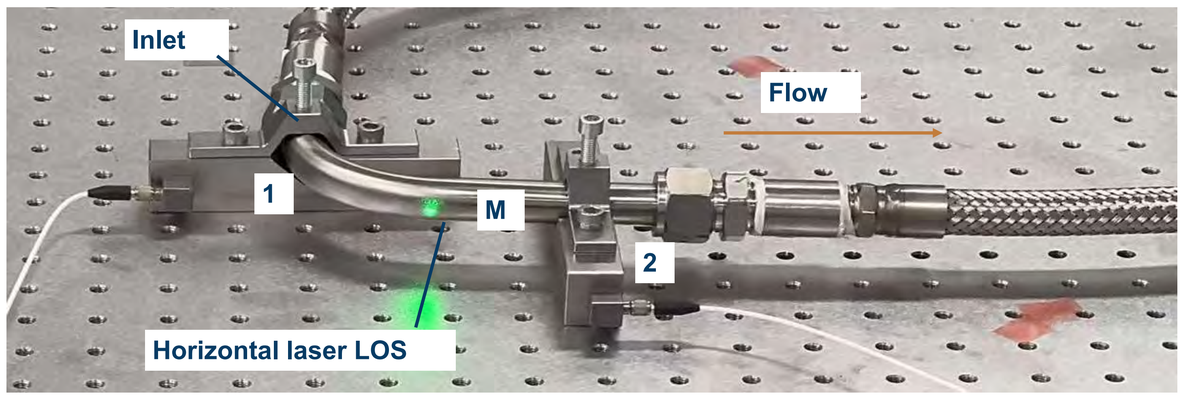


Pressure and viscous forces are integrated over the upstream, bend and downstream walls. x is out of plane; y and z are in-plane. The spectra show the frequency content and directional differences of net fluid loading. PSD: 10-500 Hz (Δf = 2 Hz). Fx/Fy/Fz RMS: 15.65/18.97/20.09 mN, from the complete demeaned records.

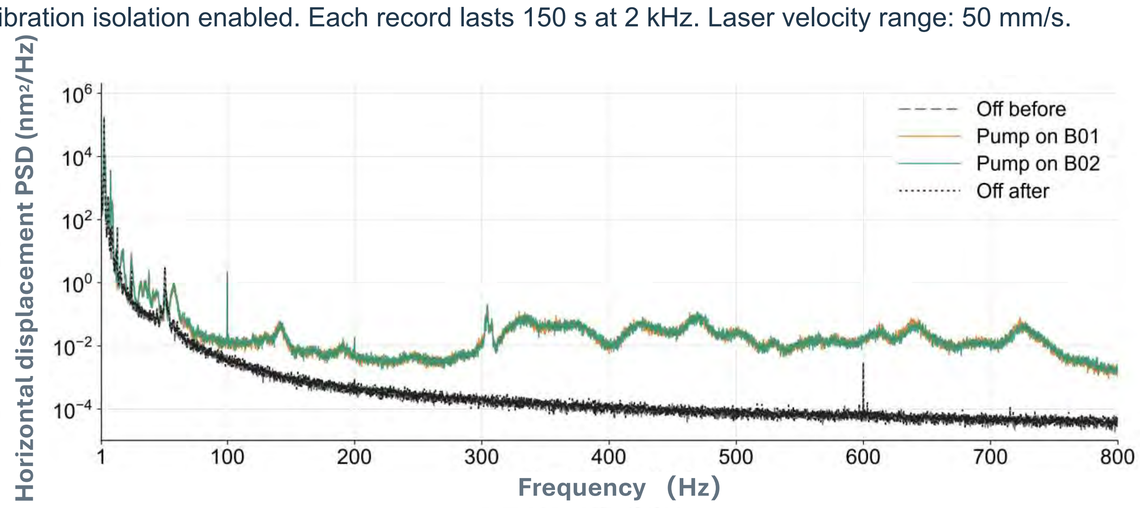
Mesh sensitivity

Mesh sensitivity was examined using 2.5, 2.0 and 1.6 mm nominal cell sizes, comparing integrated bend forces and representative wall-pressure patches. Inner-side RMS exceeded outer-side values at 30°, 45° and 60° across the meshes, while local magnitudes and the location of the highest RMS among the three inner-bend sampling points varied. Medium-to-fine bend-force RMS differences were 2.6-9.2%, relative to the finer mesh. The 2.0 mm mesh is provisionally retained, balancing these differences against 60% more cells.

3 Pipe Vibration Experiments



1/2: inlet/outlet supports; M: fixed laser spot. Velocity is measured along the horizontal line of sight (LOS) relative to the laser head. Displacement spectra are obtained by frequency-domain integration. Nominal flow rate at pump setting B: approximately 1.28-1.31 m³/h, with active vibration isolation enabled. Each record lasts 150 s at 2 kHz. Laser velocity range: 50 mm/s.



Pump-on spectra show a broadband increase, particularly above 300 Hz. The two pump-off spectra are broadly similar. The low-frequency feature near 3 Hz is also present with the pump off. PSDs were estimated using Welch's method with 10 s Hann windows, 50% overlap and a frequency spacing of 0.1 Hz.

Band-limited displacement RMS (nm)

Band (Hz)	Off before	On B01	On B02	Off after
1-100	234.554	255.987	242.162	233.838
100–800	0.435	3.768	3.761	0.447
1–800	234.555	256.014	242.191	233.838

During pump operation, a distinct narrowband peak appeared near 100 Hz, accompanied by a broadband increase, particularly above 300 Hz. The 100 Hz peak was not prominent in either pump-off record. Over 100-800 Hz, horizontal displacement RMS increased from 0.435-0.447 nm with the pump off to 3.761-3.768 nm during operation. The two consecutive pump-on records showed similar spectral features and band RMS values. After shutdown, the spectrum and band RMS returned close to the pre-operation background. Band RMS values were calculated by integrating the displacement PSD and taking the square root.

Pump-on RMS represents the total measured response, including background vibration/noise (characterized by the off-before/after records) and pump- and flow-related contributions. These contributions have not been separated; the reported RMS is not attributable to cooling-water flow alone.

4 Conclusions and Outlook

Conclusions

- HEPS QD2 measurements show reduced transverse displacement RMS over 1-100 Hz after cooling-water shutdown, indicating an association between cooling-water operation and magnet vibration.
- The preliminary LES results show spatial differences in monitored wall-pressure fluctuations, with the highest RMS at D2-I. Whole-wall force spectra characterize net loading by frequency and direction.
- At the fixed measurement point on the bent pipe, horizontal displacement RMS over 100-800 Hz was 3.76-3.77 nm during pump operation, compared with 0.44-0.45 nm with the pump off.

Next steps

1 Modal testing and model calibration: identify natural frequencies, mode shapes and damping, including support dynamics.
2 Response prediction and validation: apply distributed wall-pressure loads to a structural model matched to the test geometry and support conditions, then compare vibration at the same point, direction and flow rate.
3 Magnet-system extension: include actual cooling channels, magnet structures and supports to assess vibration mitigation.

References

[1] J. Gao, "CEPC Accelerator EDR Highlights and Collaborations," CEPC Workshop EU Edition, Lisbon (2026), slide 23.
[2] Y. Zhang et al., "Numerical and experimental investigation of cooling-water-induced vibration in HEPS magnets," RDTM (2026).